Detailed Modeling of the Low Energy Storage Quadratic Boost Converter

Oswaldo López-Santos, *Senior Member, IEEE*, Nicolás López Varón, *Student Member, IEEE*, Julio C. Rosas-Caro, *Senior Member, IEEE*, Jonathan C. Mayo-Maldonado, *Member, IEEE*, and Jesús E. Valdez-Reséndiz, *Member, IEEE*

***Abstract*—The low energy storage quadratic boost converter (LES-QBC) was recently proposed as an advantageous topology in terms of reduced output voltage ripple and fast dynamic response, besides high power density and reduced energy storage. The topological configuration can be exploited mainly through a 180° phase shift between the controlled switch gate signals. Nevertheless, this feature imposes a relevant challenge in terms of modeling, since traditional averaging an ripple estimation techniques cannot provide an accurate approximation to the actual switching dynamics of the converter. Motivated by this issue, in this article, we provide a complete quantitative analysis of both the steady-state and dynamic behavior of the LES-QBC, giving a fine understanding of their operation in continuous conduction mode when a pulse width modulator is used. The voltage gain, ripple factor, and dynamic behavior are modeled considering parasitic resistances and a wide operation range for the input voltage and the load. The demonstrated performance corroborates the high value of the converter for several applications in the industry. Every theoretical prediction is fully validated via simulations and experimental results.**

***Index Terms*—Quadratic boost converter, DC–DC power converters, modeling of power converters, pulsewidth modulation converters.**

I. Introduction

SOME renewable energy sources such as fuel cells (FCs) and photovoltaic panels have become predominant due to climate change concerns. Since they offer relatively low dc voltage levels, high step-up dc-dc converters are often used to interface them to grid-tied inverters [1]–[4]. The traditional step-up or boost converter meets practical limitations when the voltage gain is larger than five [4]–[6].

Several topologies have been proposed to overcome the challenge of the large voltage-gain in dc–dc converters. One solution is the use of large voltage-gain converters based on magnetic coupling, a transformer or a coupled inductor may be used to increase the voltage through their turns ratio [1]–[3], [7], [8], some drawbacks of this solutions are the size of the transformer, especially when the turns ratio is large, if the coupled inductor is used at the input port, it leads to discontinuous input current, and additional passive components may be required to smooth the input current waveform [4]. Another solution is the use of step-up topologies that incorporate voltage multipliers [1], [3], [5], [9], the voltage multiplier can be driven with a single transistor and used to increase the voltage gain of the converter, some disadvantages of this solution are the number of diodes may be large, in some cases, paralleling capacitors may lead to spike type of current, and additional components may be required to make it resonant, which also limits the duty cycle in which the converter may operate [10], [11]. There exist dc–dc converters composed-topologies in which the input is connected in parallel, while the output is connected in series [12]–[15].

The last type of converter that can be used to achieve large voltage gain (which is the focus of this article) is the quadratic boost converter (QBC) [16]–[24]. The traditional QBC was initially proposed in [23]; it has a simple structure and few components, organized in a nonisolated structure, similar to second-order converters. A subgroup of the known QBC topologies can be classified as cascade-type converters built from the interconnection of two identical stages. This concept can be extended for more than two stages, providing higher gains at the expense of a higher dynamic order and increasing components [22], [23].

The more recent contribution in this field introduced the low stored energy quadratic boost converter (LES-QBC). It is a nonisolated converter, similar to the traditional QBC with a different connection of capacitors and a particular pulsewidth modulation (PWM) scheme, initially introduced in [24], it implies several advantages against its traditional counterparts, such as the reduced size of the required components. For example, compared with the traditional QBC using the same parameters, the energy stored in capacitors is D2 times lower in the studied converter (LES-QBC). Due to that smaller passive components

Manuscript received March 12, 2021; revised June 19, 2021; accepted August 10, 2021. Date of publication August 16, 2021; date of current version October 15, 2021. This work was supported in part by the Ministerio de Ciencia, Tecnología e Innovación de Colombia (MinCiencias) under Contract 018–2016 and in part by the Universidad de Ibagué under project 19-529-ESP. Recommended for publication by Associate Editor J. Popovic-Gerber. *(Corresponding author: Oswaldo López-Santos.)*

Oswaldo López-Santos and Nicolás López Varón are with the Electronics Engineering Program, Universidad de Ibagué, Ibagué 730001, Colombia (e-mail: oswaldo.lopez@unibague.edu.co; 2420151035@estudiantesunibague.edu.co).

Julio C. Rosas-Caro is with the Facultad de Ingenieria, Universidad Panamericana, Mexico 03920, Mexico (e-mail: crosas@up.edu.mx).

Jonathan C. Mayo-Maldonado is with the Department of Electronic and Electrical Engineering of The University of Sheffield, Sheffield S10 2T, United Kingdom (e-mail: j.mayo@sheffield.ac.uk).

Jesús E. Valdez-Reséndiz is with the School of Engineering and Sciences, Instituto Tecnologico y de Estudios Superiores de Monterrey, Monterrey 64849, Mexico (e-mail: jesusvaldez@tec.mx).

Color versions of one or more figures in this article are available at https://doi.org/10.1109/TPEL.2021.3105081.

Digital Object Identifier 10.1109/TPEL.2021.3105081

can be used for a given specification, the dynamic response of the LES-QBC is also improved compared to the traditional QBC. Furthermore, as a consequence of the capacitor position in the power cells, the ripple of the output voltage can be considerably reduced [24]. Due to their characteristics, the LES-QBC can be used for the same applications of the traditional QBC, devices in which a voltage gain larger than five is required, and at the same time, no isolation is needed, for example, dc-based microgrids.

It is well known that the permissible ripple in dc–dc converters output voltage is the main criteria for selecting the output capacitor size. Then, the smaller the ripple component, the higher the output voltage quality and the higher the capacitance value. Consequently, an increasing capacitance implies a higher cost, and a higher printed circuit board area, affecting the converter's final cost. Beyond the aforementioned impacts on the final product, the capacitance directly relates to the time constants of the converter variables. A large capacitor represents a larger amount of energy stored, which can be seen as a detriment in the performance of the control loops. Unlike what happens in the capacitor's design for other converters, the LES -QBC has the two capacitors series-connected between the input voltage and the output voltage.

Besides the clear advantages provided by the LES-QBC, there are also emerging challenges, in particular those that require the development of new tools for analysis. For instance, the output voltage ripple behavior with respect to the duty cycle, the capacitors relation, and the output power is not evident in this new topology by following standard methods of analysis. This makes it particularly challenging to define optimal design criteria as in legacy converters. In addition, the converter is based on a suggested phase 180° shift between the control signals, yielding two operation regions for which the converter waveforms display a peculiar ripple component behavior that demands a nonconventional analysis.

In this article, we endeavor to develop such tools for analysis that are required for the accurate modeling of the voltage-ripple behavior of the LES-QBC, which naturally leads to an optimal sizing and converter design. The model is obtained from a piecewise analysis of the converter variables in continuous conduction mode (CCM). The article provides design criteria to incentivize the use of this very promising topology. The modeling of the dynamic behavior is also performed, providing a state-space representation, which can easily lead to transfer functions to apply conventional control techniques. The rest of this article is organized as follows. Complete modeling of the stationary regime of the converter operating in CCM is presented in Section II, leading to the analysis of the ripple factor (RF) behavior, which is evaluated using two numerical examples. After that, in Section III, the converter's dynamic behavior is analyzed for two numerical examples assessing the complete input voltage and power load operation range. Section IV provides simulated results obtained from PSIM software compared with experimental results obtained from two laboratory prototypes, validating the accuracy of the analysis. Finally, Section V provides the conclusions of the work.

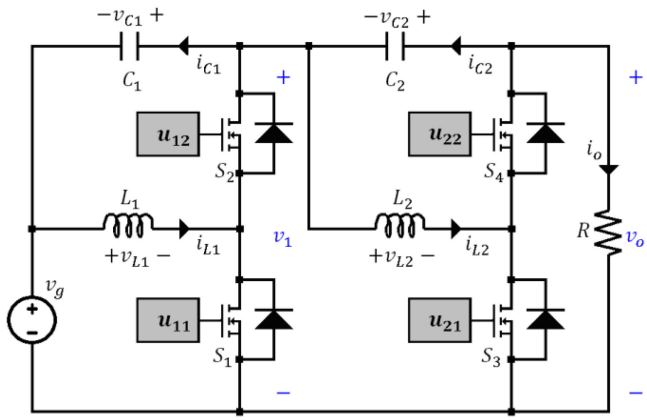

Fig. 1. Circuit diagram of the ideal LES-QBC.

II. Modeling of the Stationary Regime of the Converter

The LES-QBC shown in Fig. 1 is a fourth-order converter that is composed of two stages, each of them integrating a commutation cell (two controlled switches $S_{1,2}$ or $S_{3,4}$), one inductor connected to the input port $L_{1,2}$ and one capacitor connected between the input port and the output port $C_{1,2}$. The output voltage v_o of the converter is obtained as the sum of the input voltage v_g and the voltages of the two capacitors v_{C1} and v_{C2}. $u_{11,12,21,22}$ are the gate signals of the controlled switches.

This work considers that the converter operates in CCM, and the gate signals are produced using constant frequency PWM. The signal u_{11} has a phase shift of 180° with respect to the signal u_{21}. Consider then, that the converter can operate in four possible states (circuit structures) depending on whether the signals $u_{11,12,21,22}$ are one or zero. This generates four states defined by the pair u_1u_2 (States 10, 00, 11, and 10). The equivalent series resistance (ESR) of the capacitors are defined as R_{C1} and R_{C2} while the parasitic resistance of the inductors in series with the MOSFETs are defined as R_{E1} and R_{E2}. Nevertheless, it is worth noting that MOSFETs $S_{1,4}$ can be replaced by diodes without significant deviation from the model since it considers a constant resistance in each current path. The circuit structures corresponding to the four resulting states are depicted in Fig. 2.

It is worth mentioning that parasitic inductances and capacitances were not included in the model, since their effect in the output voltage ripple is not related to the selection of inductances and capacitances of the converter. For example, parasitic inductances may cause high-frequency ringing during the commutation and this noise can be observed in several points of the converter, but this cannot be reduced by increasing the capacitance of energy storage capacitors. It is important to reduce as possible the parasitic inductance of paths in which the current is discontinuous, but this is independent of the selection of capacitors.

Equations defining the behavior of the voltage in inductors and currents in capacitors for the four states are defined as follows:

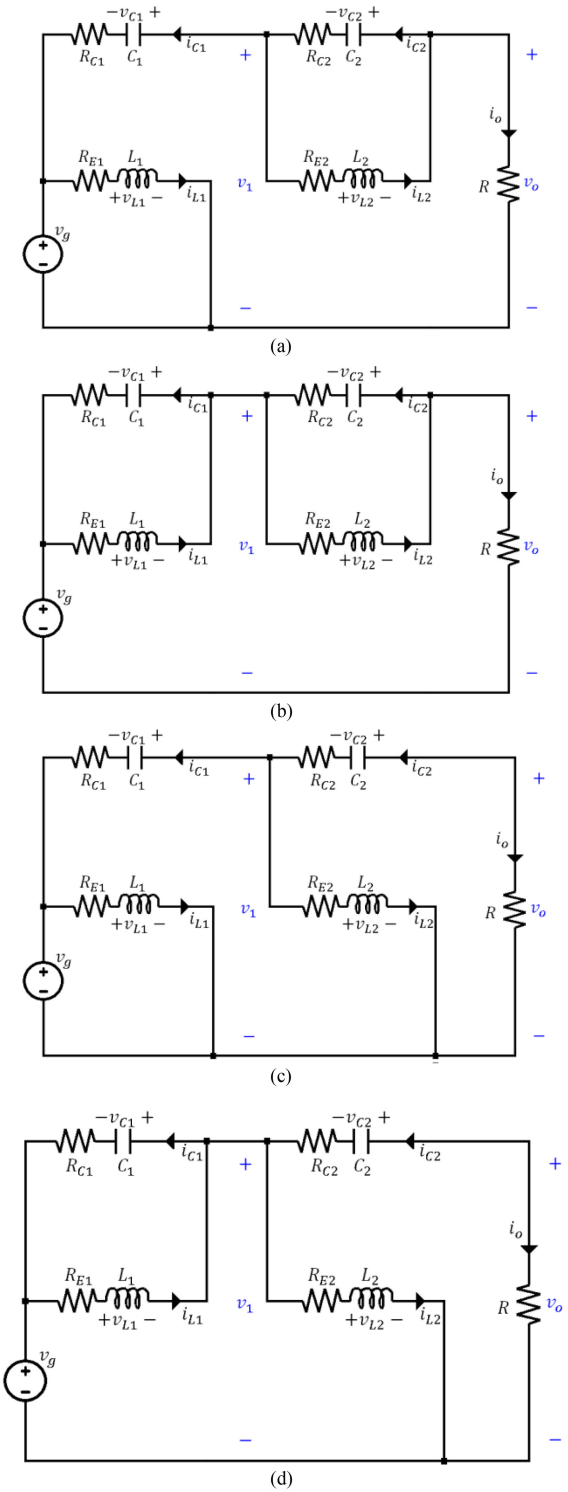

Fig. 2. Operation states of the RSE-QBC operating in CCM. (a) State 10. (b) State 00. (c) State 11. (d) State 01.

state 00 in expression (1), state 10 in expression (2), state 01 in expression (3), and state 11 in expression (4)

$$v_{L1} = v_g - i_{L1}R_{E1} - v_1$$
$$v_{L2} = v_1 - i_{L2}R_{E2} - v_o$$
$$i_{C1} = i_{L1} - i_o$$
$$i_{C2} = i_{L2} - i_o \quad (1)$$
$$v_{L1} = v_g - i_{L1}R_{E1}$$
$$v_{L2} = v_1 - i_{L2}R_{E2} - v_o$$
$$i_{C1} = -i_o$$
$$i_{C2} = i_{L2} - i_o \quad (2)$$
$$v_{L1} = v_g - i_{L1}R_{E1} - v_1$$
$$v_{L2} = v_1 - i_{L2}R_{E2}$$
$$i_{C1} = i_{L1} - i_{L2} - i_o$$
$$i_{C2} = -i_o \quad (3)$$
$$v_{L1} = v_g - i_{L1}R_{E1}$$
$$v_{L2} = v_1 - i_{L2}R_{E2}$$
$$i_{C1} = -i_{L2} - i_o$$
$$i_{C2} = -i_o. \quad (4)$$

The intermediate voltage v_1 and the output voltage v_o are defined by the following expressions:

$$v_1 = v_g + v_{C1} + R_{C1}i_{C1} \quad (5)$$
$$v_o = v_g + v_{C1} + v_{C2} + R_{C1}i_{C1} + R_{C2}i_{C2}. \quad (6)$$

A. Modeling of the Inductor Converter Waveforms

As it was mentioned before, the control signals $u_{1,2}$ are produced by a PWM enforcing a 180° phase shift between them, which originates two possible sequences of states depending on the duty cycle, which will be presented as operation regions: $D < 0.5$ and $D > 0.5$. The behavior in the boundary can be defined by evaluating the expressions for $D = 0.5$ for any of the two regions.

1) Operation Region $D < 0.5$: Operation in this region defines the sequence of states 10→00→01→00, which is presented in Fig. 3 together with the control signals and the inductor currents.

Four intervals are defined in this region: $0 < t \leq t_1$, $t_1 < t \leq T_s/2$, $T_s/2 < t \leq t_2$, and $t_2 < t \leq T_s$, being $t_1 = DT_s$ and $t_2 = (1 + 2D)\, T_s/2$. By applying the conventional volts–second and charge balances ($\text{avg}\,(v_{Lx}) = 0$ and $\text{avg}\,(i_{Cx}) = 0$), the average values of the converter variables ($I_{Lx} = \overline{i_{Lx}}$, $V_{Cx} = \overline{v_{Cx}}$) can be obtained by solving the following equations system:

$$\left[I_{L1}\ I_{L2}\ V_{C1}\ V_{C2} \right]^T = B_{D1}\, A_{D1}^{-1} \quad (7)$$

where B_{D1} and A_{D1} are defined by

$$B_{D1} = \begin{bmatrix} -V_g\,(D + K_1 D') \\ -V_g\,[D\,(1 - K_1) + (1 - K_1 - K_0)\,D'] \\ V_g K_0/R \\ V_g K_0/R \end{bmatrix}$$

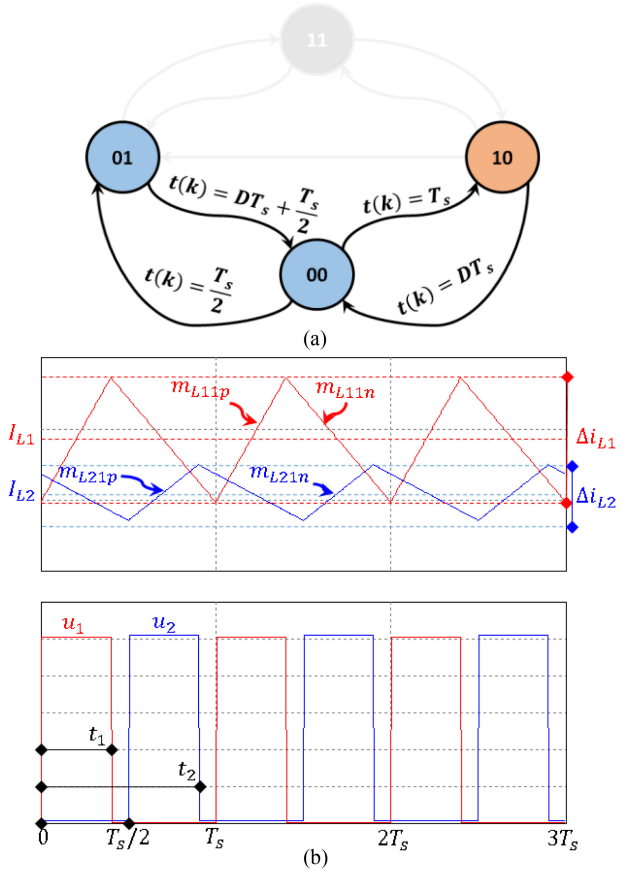

Fig. 3. Operation region D < 0.5. (a) State-flow diagram. (b) Converter waveforms.

$$A_{D1} = \begin{bmatrix} a_{D1-11} & a_{D1-12} & -(1-K_1)D' & K_1D' \\ a_{D1-21} & a_{D1-22} & 1-K_1-K_0D' & -K_1-K_0D' \\ (1-K_1)D' & a_{D1-32} & -K_0/R & -K_0/R \\ -K_1D' & a_{D1-42} & -K_0/R & -K_0/R \end{bmatrix}$$

where $D' = 1 - D$, $K_0 = \frac{R}{R+R_{C1}+R_{C2}}$, $K_1 = \frac{R_{C1}}{R}$, $K_2 = \frac{R_{C2}}{R}$, and

$$\begin{aligned} a_{D1-11} &= -R_{E1} - R_{C1}(1-K_1)D' \\ a_{D1-12} &= R_{C1}\left[(1-K_1)D + K_2(D'-D)\right] \\ a_{D1-21} &= R_{C1}\left(D' - K_1D - [K_1+K_0](D'-D)\right) \\ a_{D1-22} &= -\left[R_{E2} + R_{C1}(1-K_1)\right]D \\ &\quad -\left[R_{E2} + K_2(R_{C1}+R)\right]D' \\ a_{D1-32} &= -(1-K_1)D - K_2D' \\ a_{D1-42} &= K_1D + (1-K_2)D'. \end{aligned}$$

When operating in this region, the evolution of the circuit structures 10→00→01→00 is defined by the system equations on expressions (1)–(3). The inductor voltages are defined by the following piecewise functions:

$$v_{L1}(t) = \begin{cases} v_g - i_{L1}R_{E1} & 0 < t < T_sD \\ v_g - v_1 - i_{L1}R_{E1} & T_sD < t < T_s \end{cases} \quad (8)$$

$$v_{L2}(t) = \begin{cases} v_1 - i_{L2}R_{E2} - v_0 & 0 < t < 0.5T_s \\ v_1 - i_{L2}R_{E2} & 0.5T_s < t < t_2 \\ v_1 - i_{L2}R_{E2} - v_o & t_2 < t < T_s \end{cases} \quad (9)$$

where $t_a = 0.5T_s(1+2D)$. Each waveform interval can be rewritten in the form $v_{Lx} + i_{Lx}R_{E1} = v_z$, and then expressed as a linear differential equation of the form:

$$L_x\frac{di_{Lx}}{dt} + i_{Lx}R_{Ex} = v_z \quad (10)$$

Where the initial condition of the resulting current waveform of one interval is equal to the final value of the previous interval, following the solution method presented in Appendix 1 (see for details), the waveforms of the inductor currents are synthesized as defined by (11) and (12):

$$i_{L1} = \begin{cases} f_{11a}(t) & 0 < t \le DT_s \\ f_{11b}(t) & DT_s < t \le T_s \end{cases} \quad (11)$$

$$i_{L2} = \begin{cases} f_{12a}(t) & 0 < t \le T_s/2 \\ f_{12b}(t) & 0.5T_s < t < t_a \\ f_{12c}(t) & t_a < t \le T_s \end{cases} \quad (12)$$

where

$$\begin{aligned} f_{11a}(t) &= \frac{V_g}{R_{E1}} - \left(\frac{V_g}{R_{E1}} - i_{L1_a}(0)\right)e^{-\frac{R_{E1}}{L_1}t} \\ f_{11b}(t) &= \frac{-V_{C1}}{R_{E1}} + \left(\frac{V_{C1}}{R_{E1}} + i_{L1_b}(0)\right)e^{-\frac{R_{E1}}{L_1}t} \\ f_{12a}(t) &= \frac{-V_{C2}}{R_{E2}} + \left(\frac{V_{C2}}{R_{E2}} + i_{L2_a}(0)\right)e^{-\frac{R_{E2}}{L_2}t} \\ f_{12b}(t) &= \frac{V_1}{R_{E2}} - \left(\frac{V_1}{R_{E2}} - i_{L2_b}(0)\right)e^{-\frac{R_{E2}}{L_2}t} \\ f_{12c}(t) &= \frac{V_{C2}}{R_{E2}} + \left(\frac{V_{C2}}{R_{E2}} + i_{L2_c}(0)\right)e^{-\frac{R_{E2}}{L_2}t}. \end{aligned}$$

Also, as it is developed in Appendix I, the following nonlinear terms are defined:

$$S_1 = 0.5 - 0.5sign(t - DT_s) \quad (13)$$

$$S_2 = 0.5 - 0.5sign(t - T_s/2) \quad (14)$$

$$S_3 = 0.5 - 0.5sign\left(t - \frac{T_s}{2} - DT_s\right). \quad (15)$$

Then, from (1)–(3) and (11)–(15), the capacitor currents waveforms can be obtained as follows:

$$i_{C1} = (S_3 - S_1)\,f_{11b} - (S_3 - S_2)\,f_{12b} - \frac{V_o}{R} \quad (16)$$

$$i_{C2} = S_2\,f_{12a} + (1 - S_3)\,f_{12c} - \frac{V_o}{R}. \quad (17)$$

The voltage waveforms of the capacitors are obtained by using expressions (18) and (19) where any bias of the ac component

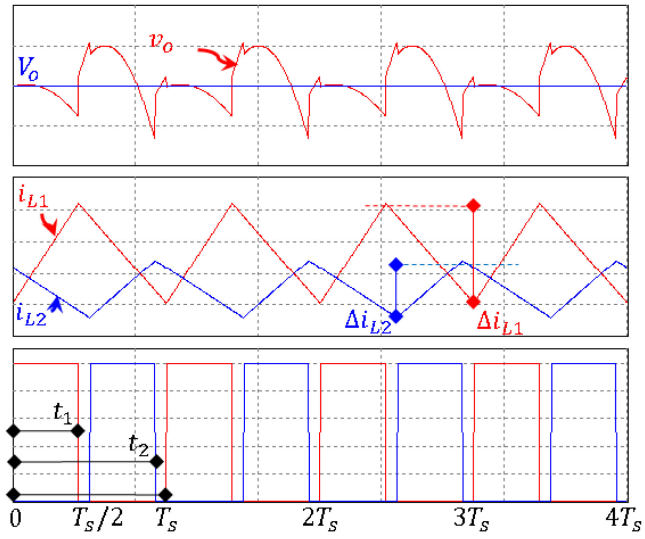

Fig. 4. Detail of the converter waveforms and intervals for D = 0.4.

is eliminated before adding it to the average component

$$v_{C1} = V_{C1} + \underbrace{\int_0^{T_s} i_{C1}dt - \frac{1}{T_s}\int_0^{T_s}\left(\int_0^{T_s} i_{C1}dt\right)dt}_{\text{AC component}} \quad (18)$$

$$v_{C2} = V_{C2} + \underbrace{\int_0^{T_s} i_{C2}dt - \frac{1}{T_s}\int_0^{T_s}\left(\int_0^{T_s} i_{C2}dt\right)dt}_{\text{AC component}}. \quad (19)$$

Recalling (6), $v_o = v_g + v_{C1} + v_{C2} + R_{C1}i_{C1} + R_{C2}i_{C2}$. Fig. 4 details the ripple of the inductor's current and output voltage waveforms related to gate signals and time intervals for the case $D = 0.4$.

2) Operation Region D > 0.5: This structure is obtained during intervals in which M_1 and M_2 are closed ($u_1 = 1, u_2 = 1$), and consequently D_1 and D_2 are open. A state-flow diagram describing the sequence obtained in this region (11→01→11→10) is presented in Fig. 5 together with the control signals and the inductor currents.

Like in the precedent region, four intervals results defined in this region: $0 < t \le t_1$, $t_1 < t \le 0.5T_s$, $0.5T_s < t \le t_2$, and $t_2 < t \le T_s$, being $t_1 = (D - 0.5)\ T_s$ and $t_2 = DT_s$. By applying the same procedure of the previous region, it is obtained that

$$\left[I_{L1}\ I_{L2}\ V_{C1}\ V_{C2}\right]^T = B_{D2}\ A_{D2}^{-1} \quad (20)$$

having B_{D2} and A_{D2} defined by

$$B_{D1} = \begin{bmatrix} -V_g\left(D + K_1D'\right) \\ -V_g\left[\left(1-K_1\right)D + \left(1-K_1-K_0\right)D'\right] \\ V_gK_0/R \\ V_gK_0/R \end{bmatrix}$$

$$A_{D2} =$$

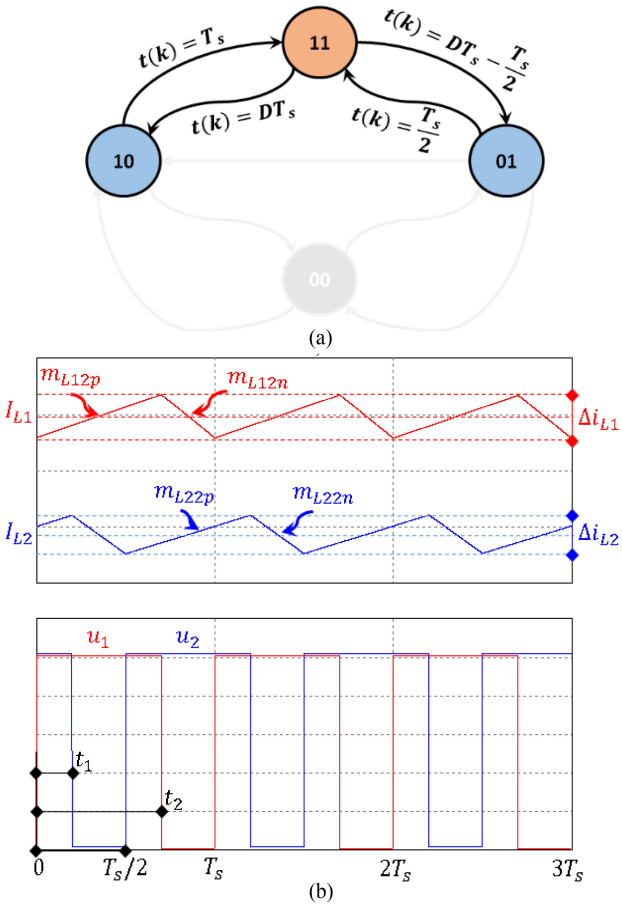

Fig. 5. Operation region D > 0.5. (a) State-flow diagram. (b) Converter waveforms.

$$\begin{bmatrix} a_{D2-11} & a_{D2-12} & -\left(1-K_1\right)D' & K_1D' \\ a_{D2-21} & a_{D2-22} & 1-K_1-K_0D' & -K_1-K_0D' \\ \left(1-K_1\right)D' & a_{D2-32} & -G_x & -G_x \\ -K_1D' & a_{D2-42} & -G_x & -G_x \end{bmatrix}$$

where

$$\begin{aligned} a_{D2-11} &= -R_{E1} - R_{C1}\left(1-K_1\right)D' \\ a_{D2-12} &= R_{C1}\ \left(1-K_1\right)D' \\ a_{D2-21} &= R_{C1}\ \left(1-K_1\right)D' \\ a_{D2-22} &= -\left[R_{E2} + R_{C1}\left(1-K_1\right)\right]D \\ &\quad -\left[R_{E2} + K_2\left(R_{C1}+R\right)\right] \\ a_{D2-32} &= -\left(1-K_1\right)D - K_2D' \\ a_{D2-42} &= K_1\ \left(2D'-D\right) + \left(1-K_2\right)D'. \end{aligned}$$

Now, considering the above-defined intervals and expressions in Table I, the waveforms of the inductor currents can be synthesized as follows:

$$i_{L1} = \begin{cases} f_{21a}\left(t\right)\ 0 < t \le DT_s \\ f_{21b}\left(t\right)\ DT_s < t \le T_s \end{cases} \quad (21)$$

TABLE I
PARAMETERS OF NUMERIC EXAMPLE 1

Element	Symbol	Value	Unities
Capacitor Cell 1	C_1	2,2 3.3 4,7 11 22 47 82	μF
	R_{C1}	50	$m\Omega$
Capacitor Cell 2	C_2	11	μF
	R_{C2}	50	$m\Omega$
Inductor Cell 1	L_1	1.80	mH
	R_{E1}	200	$m\Omega$
Inductor Cell 2	L_2	6.08	mH
	R_{E2}	200	$m\Omega$
Load resistance	R_{min}	240	Ω
	R_{max}	2400	Ω
Switching frequency	f_s	27	kHz

$$i_{L2} = \begin{cases} f_{22a}(t) & 0 < t \le t_1 \\ f_{22b}(t) & t_1 < t \le T_s/2 \\ f_{22c}(t) & T_s/2 < t \le T_s \end{cases} \quad (22)$$

where

$$f_{22a}(t) = \frac{V_1}{R_{E2}} - \left(\frac{V_1}{R_{E2}} - i_{L2_a}(0)\right) e^{-\frac{R_{E2}}{L_2}t}$$
$$f_{22b}(t) = \frac{-V_{C2}}{R_{E2}} + \left(\frac{V_{C2}}{R_{E2}} + i_{L2_b}(0)\right) e^{-\frac{R_{E2}}{L_2}t}$$
$$f_{22c}(t) = \frac{V_1}{R_{E2}} - \left(\frac{V_1}{R_{E2}} - i_{L2_c}(0)\right) e^{-\frac{R_{E2}}{L_2}t}.$$

Then, from (10) and (11), the capacitor currents waveforms can be obtained from Table I as follows:

$$i_{C1} = (1 - S_3)\ f_{11b} - S_1 f_{22a} - (S_3 - S_2)\, f_{22c} - \frac{V_o}{R} \quad (23)$$

$$i_{C2} = (S_2 - S_1)\ f_{22b} - \frac{V_o}{R}. \quad (24)$$

The voltage waveforms of the capacitors are obtained by using the same expressions (18) and (19) solved for (23) and (24). Fig. 6 details the ripple in the inductor currents and output voltage waveforms related with gate signals and time intervals for the case $D = 0.6018$.

B. Output Voltage Ripple Analysis

A quantitative analysis of the ripple behavior of the converter can be performed by using the RF or the peak-to-peak ripple (Rpp) indicators. Consider that output voltage waveform is defined by

$$v_o = V_{dc} + \tilde{v}_o \quad (25)$$

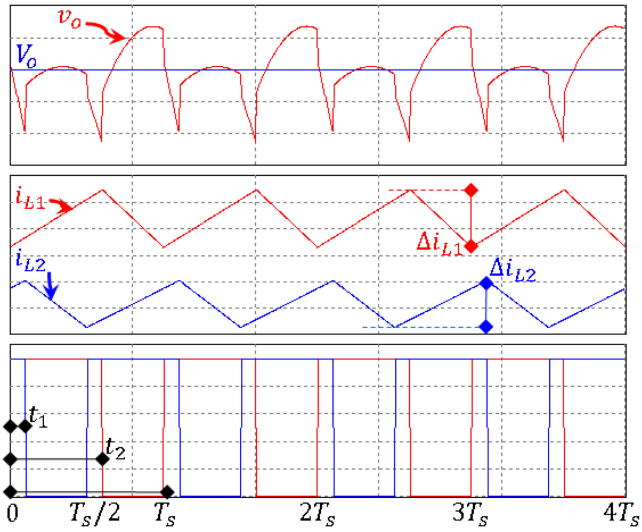

Fig. 6. Detail of the converter waveforms and intervals for D = 0.6.

where V_{dc} is the average output voltage and $v_{ac}(\omega t)$ is its ripple component. Also consider that maximum and minimum of the output voltage are defined as $\max(v_o)$ and $\min(v_o)$.

Then, the RF is defined as follows:

$$RF = \frac{\tilde{v}_{orms}}{V_{dc}}$$

wherein both $\tilde{v}_{orms}$ and V_{dc} are functions of the operation point (duty cycle) which in turn is defined by the input voltage and output load conditions. The RF can be computed as follows:

$$RF = \frac{1}{V_{dc}} \sqrt{\frac{1}{T_s} \int_0^{Ts} v_o^2 dt - V_{dc}^2}. \quad (26)$$

Conversely, considering the symmetry of the ac component, the peak ripple indicator Rpp can be computed as

$$Rpp = \frac{\max(v_o) - \min(v_o)}{2V_{dc}}. \quad (27)$$

To better understand the correlation between both indicators, we provide numerical examples.

C. Numerical Example 1

Consider an RSE-QBC of 240 W, which is used to provide an output voltage of 240 V from a series battery bank of five 12 V batteries whose voltage ranges from 50 to 72 V. The better features must be guaranteed for the neighbor of a nominal input voltage of 60 V. The converter feds a resistive load demanding a power consumption between the 24 and 240 W (10% to 100% of the nominal power).

Consider that switching frequency is defined as 27 kHz and the inductor design is constrained to attain boundary conduction mode (BCM) when the minimum power load is fed by the converter (current ripple amplitude is 200% of the average value of the inductor current at the operation point defining the minimum average current). From (2)–(4), by replacing $v_{Lx} = L\frac{\Delta i_{Lx}}{\Delta t}$ and average values for voltages computed using (7) or (20), the

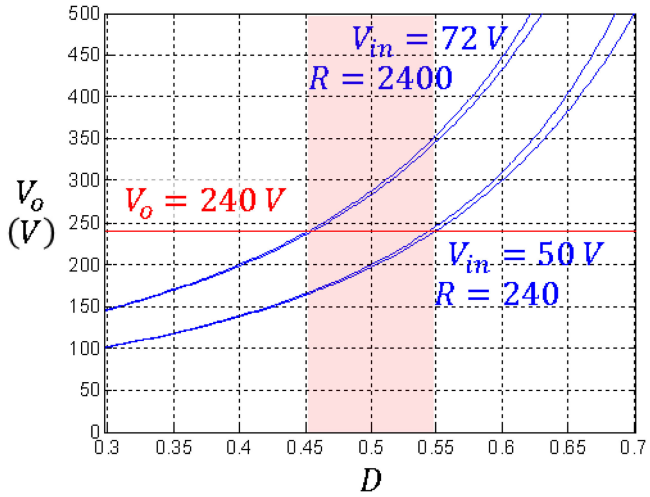

Fig. 7. Delimitation of the duty cycle range for numerical example 1.

following expressions are obtained for inductor design:

$$L_1 = \frac{{V_{g\ \max}}^2}{2P_{\min}\ f_s}\left(1 - \sqrt{\frac{V_{g\ \max}}{V_o}}\right) \tag{28}$$

$$L_2 = \frac{V_{g\ \max} V_o}{2P_{\min}\ f_s}\left(1 - \sqrt{\frac{V_{g\ \max}}{V_o}}\right). \tag{29}$$

A value for C_2 similar to the one required to ensure a RF below 1% at the output of the conventional QBC using the same parameters was selected. Different values of C_1 are selected for further analysis. In this example, the parameters listed in Table I are used for simulations.

First, the steady-state values of the converter variables are computed for the entire range of duty cycle using expressions (7) and (20) considering the maximum and minimum load. As it can be observed in Fig. 7, the desired voltage of 240 V is obtained using a duty cycle ranging from 0.4 to 0.6.

For the proposed converter, further analysis is required to adequately select the appropriate capacitors. To provide useful results, the RF and Rpp percentage were evaluated considering $C_1 = C_2 = 11\ \mu$F.

As it can be noted in Fig. 8, the converter is able to supply the desired 240 V output voltage in the entire range of input voltages using a duty cycle ranging from 0.45 to 0.55. The RF shows its better performance for the operation region around $D \approx 0.5$, which corresponds to input voltages around 60 V. When the converter operates at low output power, the RF is practically similar for the entire range of voltage while for the rated power it describes a parabolic behavior. Operating with the rated power (240 W), the RF is lower than 0.12% taking its minimum value around 0.03%. The Rpp shows a similar behavior but a difference between both operation regions can be identified. Operating with the rated power (240 W), the RF is lower than 0.6% taking its minimum value around 0.1%.

Finally, the ripple behavior was evaluated considering different relations of the capacitor size and the extremes of the output power. As it is depicted in Fig. 9(a) for low powers, values of

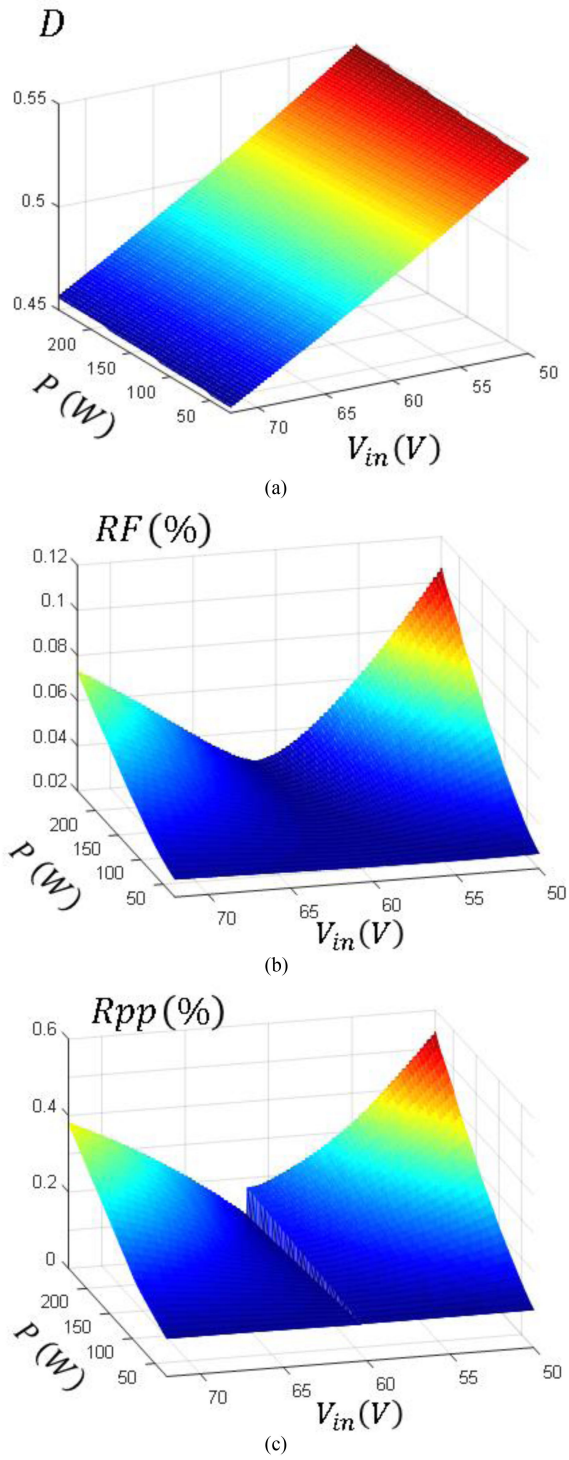

Fig. 8. Operation region of the LSW-QBC of the numerical example 1. (a) Duty cycle. (b) RF. (c) Rpp percentage.

C_1 lower than C_2 considerably increases the RF while values of C_1 higher than C_2 has not considerable effect. In Fig. 9(b), similar to what happens for low powers, values of C_1 lower than C_2 considerably increases the RF. Furthermore, the use of capacitors of the same value ensures, in this example, a better result showing a reduced RF. After that, as it is depicted in Fig. 9(c), for values of C_1 higher than C_2, the RF increases.

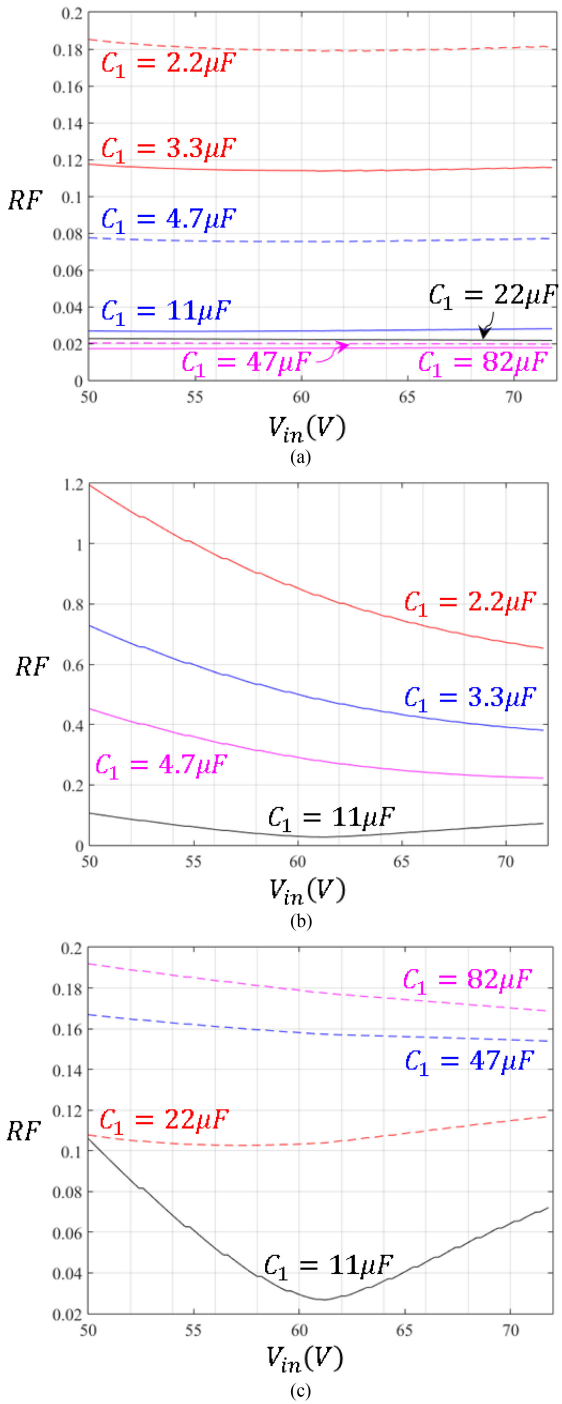

Fig. 9. RF as a function of the input voltage for numerical example 1. (a) Minimum power (24 W). (b) Maximum power for relations $C_1 \geq C_2$ (240 W). (c) Maximum power for relations $C_1 \leq C_2$.

This last result show how the potential use of the best features of the converter is related with operation with duty cycles close than 0.5 and having $C_1 = C_2$.

D. Numerical Example 2

Consider an RSE-QBC of 600 W, which will be used to provide an output voltage of 380 V from a battery bank of five 12 V batteries connected in series. Wide which voltage ranges from 50 to 72 V. The best properties must be guaranteed for the neighbor of a nominal input voltage of 60 V. The converter feds a resistive load demanding a power consumption between 60 and 600 W (10% to 100% of the nominal power). Consider that switching frequency is defined as 50 kHz and the inductor design is constrained to attain BCM when the minimum power load is fed by the converter. The parameters listed in Table II are used for numerical analysis.

TABLE II
PARAMETERS OF NUMERIC EXAMPLE 2

Element	Symbol	Value	Unities
Capacitor Cell 1	C_1	*2,2*	μF
		3.3	
		4,7	
		11	
		22	
		47	
		82	
	R_{C1}	*50*	$m\Omega$
Capacitor Cell 2	C_2	*11*	μF
	R_{C2}	*50*	$m\Omega$
Inductor Cell 1	L_1	*487.9*	μH
	R_{E1}	*200*	$m\Omega$
Inductor Cell 2	L_2	*2.57*	mH
	R_{E2}	*200*	$m\Omega$
Load resistance	R_{min}	*240*	Ω
	R_{max}	*2400*	Ω
Switching frequency	f_s	*50*	kHz

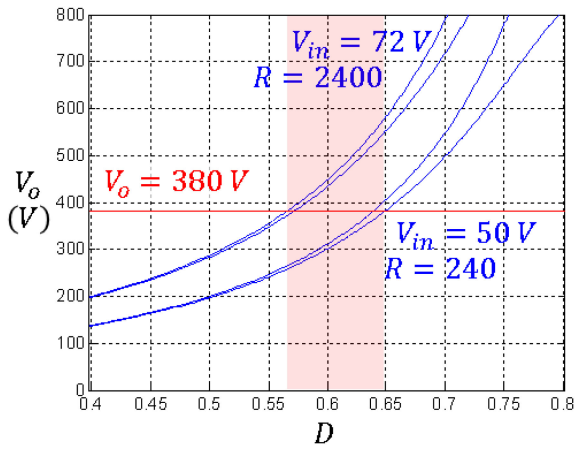

Fig. 10. Delimitation of the duty cycle range for numerical example 2.

The steady-state values of the converter variables are computed for the entire range of duty cycle using expressions (7) and (20) considering the maximum and minimum load. As it can be observed in Fig. 10, the desired voltage of 380 V is obtained using duty cycle ranging from 0.56 to 0.65.

Different to the numerical example 1, in this case, the range of operation of the converter has not included the critical point of $D \approx 0.5$. As it is possible to observe in Fig. 11, the duty cycle

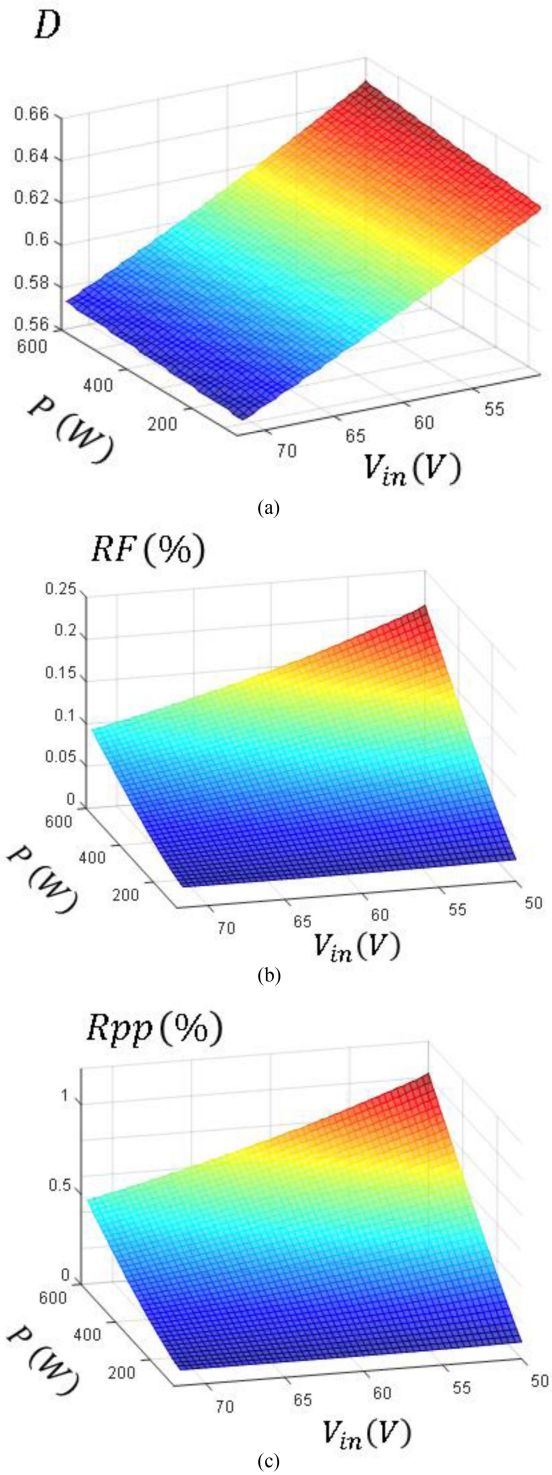

Fig. 11. Operation region of the LSW-QBC of the numerical example 1. (a) Duty cycle. (b) RF. (c) Rpp percentage.

takes values above 0.56. From the analysis, it is possible to conclude that both RF and Rpp have a similar behavior. The values of RF observed for converter operating with minimum power are similar indistinctly to the input voltage value. Conversely, operating with the maximum power, the RF increases when the input voltage decreases.

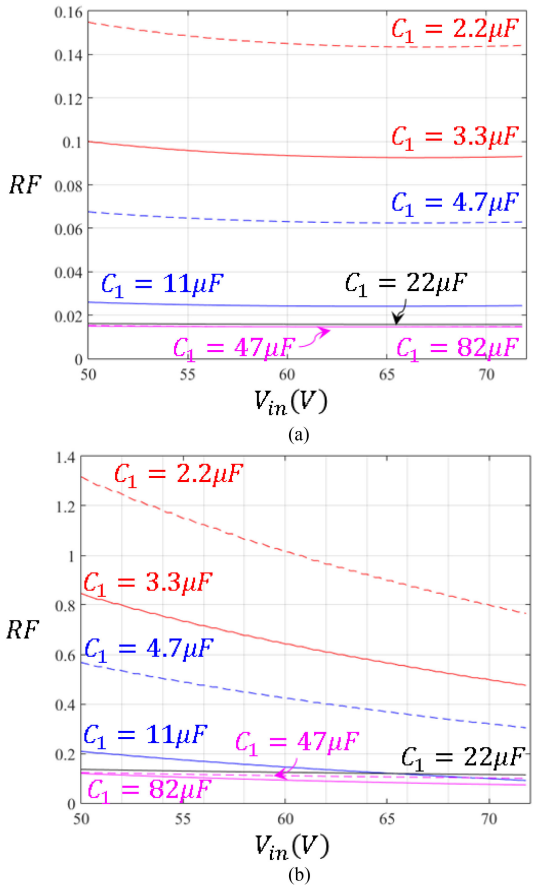

Fig. 12. RF as a function of the input voltage for numerical example 2. (a) Minimum power. (b) Maximum power.

Similar to the previous example, the ripple behavior was evaluated considering different relations of the capacitor sizes. As it is depicted in Fig. 12, values of C_1 lower than C_2 considerably increases the RF. The use of capacitor of the same value ensures in this example the better tradeoff because although a lower ripple is obtained with a higher value of C_1, that reduction is not compared with the required size of the capacitor. According to the results, similar RF is obtained when $C_1 = 11\,\mu$F or $C_1 = 82\,\mu$F.

III. Dynamic Modeling of the Converter

A. Derivation of the Linear Averaged State-Space Model

The expressions (1)–(4) can be written in the differential form to obtain the dynamic model for each operating state of the converter as follows: State 00 in expression (30), state 10 in expression (31), state 01 in expression (32), and state 11 in expression (33)

$$\frac{di_{L1}}{dt} = \frac{1}{L_1}\left[-\left(K_a R_{C1} + R_{E1}\right) i_{L1} + K_1 K_o R_{C2} i_{L2} - K_a v_{C1} + K_1 K_o v_{C2} + K_1 K_o v_g\right]$$

$$\frac{di_{L2}}{dt} = \frac{1}{L_2}\left[K_c R_{C1} i_{L1} - \left(K_b R_{C2} + R_{E2}\right) i_{L2} + K_c v_{C1} - K_b v_{C2} + K_c v_g\right]$$

$$
\begin{aligned}
\frac{dv_{C1}}{dt} &= \frac{1}{RC_1}\left[\left(R-K_oR_{C1}\right)i_{L1}-K_oR_{C2}i_{L2}\right.\\
&\quad \left.-K_ov_{C1}-K_ov_{C2}-K_ov_g\right]\\
\frac{dv_{C2}}{dt} &= \frac{1}{RC_2}\left[-K_oR_{C1}i_{L1}+\left(R-K_oR_{C2}\right)i_{L2}-K_ov_{C1}\right.\\
&\quad \left.-K_ov_{C2}-K_ov_g\right]\\
v_1 &= K_aR_{C1}i_{L1}-K_1K_oR_{C2}i_{L2}+K_av_{C1}-K_1K_ov_{C2}\\
&\quad +K_av_g\\
v_o &= K_oR_{C1}i_{L1}+K_oR_{C2}i_{L2}+K_ov_{C1}+K_ov_{C2}+K_ov_g
\end{aligned}
\tag{30}
$$

$$
\begin{aligned}
\frac{di_{L1}}{dt} &= \frac{1}{L_1}\left(-R_{E1}i_{L1}+v_g\right)\\
\frac{di_{L2}}{dt} &= \frac{1}{L_2}\left[-\left(K_bR_{C2}+R_{E2}\right)i_{L2}+K_cv_{C1}\right.\\
&\quad \left.-K_bv_{C2}+K_cv_g\right]\\
\frac{dv_{C1}}{dt} &= \frac{1}{RC_1}\left(-K_oR_{C2}i_{L2}-K_ov_{C1}-K_ov_{C2}-K_ov_g\right)\\
\frac{dv_{C2}}{dt} &= \frac{1}{RC_2}\left[\left(R-K_oR_{C2}\right)i_{L2}-K_ov_{C1}-K_ov_{C2}-K_ov_g\right]\\
v_1 &= -K_1K_oR_{C2}i_{L2}+K_av_{C1}-K_1K_ov_{C2}+K_av_g\\
v_o &= K_oR_{C2}i_{L2}+K_ov_{C1}+K_ov_{C2}+K_ov_g
\end{aligned}
\tag{31}
$$

$$
\begin{aligned}
\frac{di_{L1}}{dt} &= \frac{1}{L_1}\left[-\left(K_aR_{C1}+R_{E1}\right)i_{L1}+K_aR_{C1}i_{L2}\right.\\
&\quad \left.-K_av_{C1}+K_1K_ov_{C2}+K_1K_ov_g\right]\\
\frac{di_{L2}}{dt} &= \frac{1}{L_2}\left[K_aR_{C1}i_{L1}-\left(K_aR_{C1}+R_{E2}\right)i_{L2}\right.\\
&\quad \left.+K_av_{C1}-K_1K_ov_{C2}+K_av_g\right]\\
\frac{dv_{C1}}{dt} &= \frac{1}{RC_1}\left[\left(R-K_oR_{C1}\right)i_{L1}-\left(R-K_oR_{C1}\right)i_{L2}\right.\\
&\quad \left.-K_ov_{C1}-K_ov_{C2}-K_ov_g\right]\\
\frac{dv_{C2}}{dt} &= \frac{1}{RC_2}\left[-K_oR_{C1}i_{L1}+K_oR_{C1}i_{L2}-K_ov_{C1}\right.\\
&\quad \left.-K_ov_{C2}-K_ov_g\right]\\
v_1 &= K_aR_{C1}i_{L1}-K_aR_{C1}i_{L2}+K_av_{C1}-K_1K_ov_{C2}+K_av_g\\
v_o &= K_oR_{C1}i_{L1}-K_oR_{C1}i_{L2}+K_ov_{C1}+K_ov_{C2}+K_ov_g
\end{aligned}
\tag{32}
$$

$$
\begin{aligned}
\frac{di_{L1}}{dt} &= \frac{1}{L_1}\left[-R_{E1}i_{L1}+v_g\right]\\
\frac{di_{L2}}{dt} &= \frac{1}{L_2}\left[-\left(K_aR_{C1}+R_{E2}\right)i_{L2}+K_av_{C1}\right.\\
&\quad \left.-K_1K_ov_{C2}+K_av_g\right]\\
\frac{dv_{C1}}{dt} &= \frac{1}{RC_1}\left[-\left(R-K_oR_{C1}\right)i_{L2}-K_ov_{C1}-K_ov_{C2}\right.\\
&\quad \left.-K_ov_g\right]\\
\frac{dv_{C2}}{dt} &= \frac{1}{RC_2}\left[K_oR_{C1}i_{L2}-K_ov_{C1}-K_ov_{C2}-K_ov_g\right]\\
v_1 &= -K_aR_{C1}i_{L2}+K_av_{C1}-K_1K_ov_{C2}+K_av_g\\
v_o &= -K_oR_{C1}i_{L2}+K_ov_{C1}+K_ov_{C2}+K_ov_g
\end{aligned}
\tag{33}
$$

where $K_a = 1-K_1K_o$, $K_b = K_o\,(1+K_1)$, and $K_c = 1-K_b = K_a - K_0$. The differential model defined by expressions (30)–(33) can be represented in the state-space using the following sets of matrices, respectively:

$$
A_{00} = \begin{bmatrix}
\frac{-K_aR_{C1}-R_{E1}}{L_1} & \frac{K_1K_oR_{C2}}{L_1} & \frac{-K_a}{L_1} & \frac{K_1K_o}{L_1}\\
\frac{K_cR_{C1}}{L_2} & \frac{-K_bR_{C2}-R_{E2}}{L_2} & \frac{K_c}{L_2} & \frac{-K_b}{L_2}\\
\frac{R-K_oR_{C1}}{RC_1} & \frac{-K_oR_{C2}}{RC_1} & \frac{-K_o}{RC_1} & \frac{-K_o}{RC_1}\\
\frac{-K_oR_{C1}}{RC_2} & \frac{R-K_oR_{C2}}{RC_2} & \frac{-K_o}{RC_2} & \frac{-K_o}{RC_2}
\end{bmatrix}
$$

$$
B_{00} = \begin{bmatrix}
\frac{K_1K_o}{L_1}\\
\frac{K_c}{L_2}\\
\frac{-K_o}{RC_1}\\
\frac{-K_o}{RC_2}
\end{bmatrix}
\qquad
D_{00} = \begin{bmatrix}
0\\0\\K_a\\K_o
\end{bmatrix}
$$

$$
C_{00} = \begin{bmatrix}
1 & 0 & 0 & 0\\
0 & 1 & 0 & 0\\
K_aR_{C1} & -K_1K_oR_{C2} & K_a & -K_1K_o\\
K_oR_{C1} & K_oR_{C2} & K_o & K_o
\end{bmatrix}
\tag{34}
$$

$$
A_{10} = \begin{bmatrix}
\frac{-R_{E1}}{L_1} & 0 & 0 & 0\\
0 & \frac{-K_bR_{C2}-R_{E2}}{L_2} & \frac{K_c}{L_2} & \frac{-K_b}{L_2}\\
0 & \frac{-K_oR_{C2}}{RC_1} & \frac{-K_o}{RC_1} & \frac{-K_o}{RC_1}\\
0 & \frac{R-K_oR_{C2}}{RC_2} & \frac{-K_o}{RC_2} & \frac{-K_o}{RC_2}
\end{bmatrix}
$$

$$
B_{10} = \begin{bmatrix}
\frac{1}{L_1}\\
\frac{K_c}{L_2}\\
\frac{-K_o}{RC_1}\\
\frac{-K_o}{RC_2}
\end{bmatrix}
\qquad
D_{10} = \begin{bmatrix}
0\\0\\K_a\\K_o
\end{bmatrix}
$$

$$C_{10}=\begin{bmatrix}1 & 0 & 0 & 0\\ 0 & 1 & 0 & 0\\ 0 & -K_1K_oR_{C2} & K_a & -K_1K_o\\ 0 & K_oR_{C2} & K_o & K_o\end{bmatrix} \tag{35}$$

$$A_{01}=\begin{bmatrix}\frac{-K_aR_{C1}-R_{E1}}{L_1} & \frac{K_aR_{C1}}{L_1} & \frac{-K_a}{L_1} & \frac{K_1K_o}{L_1}\\ \frac{K_aR_{C1}}{L_2} & \frac{-K_aR_{C1}-R_{E2}}{L_2} & \frac{K_a}{L_2} & \frac{-K_1K_0}{L_2}\\ \frac{R-K_oR_{C1}}{RC_1} & \frac{-R+K_oR_{C1}}{RC_1} & \frac{-K_o}{RC_1} & \frac{-K_o}{RC_1}\\ \frac{-K_oR_{C1}}{RC_2} & \frac{K_oR_{C1}}{RC_2} & \frac{-K_o}{RC_2} & \frac{-K_o}{RC_2}\end{bmatrix}$$

$$B_{01}=\begin{bmatrix}\frac{K_1K_o}{L_1}\\ \frac{K_a}{L_2}\\ \frac{-K_o}{RC_1}\\ \frac{-K_o}{RC_2}\end{bmatrix}\quad D_{01}=\begin{bmatrix}0\\ 0\\ K_a\\ K_o\end{bmatrix}$$

$$C_{01}=\begin{bmatrix}1 & 0 & 0 & 0\\ 0 & 1 & 0 & 0\\ K_aR_{C1} & -K_aR_{C1} & K_a & -K_1K_o\\ K_oR_{C1} & -K_oR_{C1} & K_o & K_o\end{bmatrix} \tag{36}$$

$$A_{11}=\begin{bmatrix}\frac{-R_{E1}}{L_1} & 0 & 0 & 0\\ 0 & \frac{-K_aR_{C1}-R_{E2}}{L_2} & \frac{K_a}{L_2} & \frac{-K_1K_0}{L_2}\\ 0 & \frac{-R+K_oR_{C1}}{RC_1} & \frac{-K_o}{RC_1} & \frac{-K_o}{RC_1}\\ 0 & \frac{K_oR_{C1}}{RC_2} & \frac{-K_o}{RC_2} & \frac{-K_o}{RC_2}\end{bmatrix}$$

$$B_{11}=\begin{bmatrix}\frac{1}{L_1}\\ \frac{K_a}{L_2}\\ \frac{-K_o}{RC_1}\\ \frac{-K_o}{RC_2}\end{bmatrix}\quad D_{11}=\begin{bmatrix}0\\ 0\\ K_a\\ K_o\end{bmatrix}$$

$$C_{11}=\begin{bmatrix}1 & 0 & 0 & 0\\ 0 & 1 & 0 & 0\\ 0 & -K_aR_{C1} & K_a & -K_1K_o\\ 0 & -K_oR_{C1} & K_o & K_o\end{bmatrix}. \tag{37}$$

As it is well known in the literature, the dynamic behavior of the dc–dc power converters operating in CCM using PWM can be accurately modeled by using averaged linear models which in turn are derived from the state-space representation [15]. As a particular condition for the studied converter operating in CCM, its structure changes between three of the four possible states and one of these states changes depending on the instantaneous value of the duty cycle. Then, an extension of the conventional procedure is applied to obtain the averaged linear models.

1) Operation Region D<0.5: Considering the sequence of states 10→ 00→10→00, the following equation system is obtained from the region D<0.5:

$$\begin{aligned}\frac{d\tilde{x}}{dt}&=\left[D\left(A_{10}+A_{01}\right)+\left(1-2D\right)A_{00}\right]\tilde{x}\\ &\quad+\left[\left(A_{10}+A_{01}-2A_{00}\right)X+\left(B_{10}+B_{01}-2B_{00}\right)V_g\right]\tilde{d}\\ &\quad+\left(D\left(B_{10}+B_{01}\right)+\left(1-2D\right)B_{00}\right)\tilde{v}_g\\ y&=\left[D\left(C_{10}+C_{01}\right)+\left(1-2D\right)C_{00}\right]\tilde{x}\\ &\quad+\left[\left(C_{10}+C_{01}-2C_{00}\right)X+\left(D_{10}+D_{01}-2D_{00}\right)V_g\right]\tilde{d}\\ &\quad+\left(D\left(D_{10}+D_{01}\right)+\left(1-2D\right)D_{00}\right)\tilde{v}_g\end{aligned} \tag{38}$$

where $\tilde{d}$ is defined as the control variable and $\tilde{v}_g$ as a disturbance.

2. Operation Region D > 0.5: Considering the sequence of states 11→10→11→01, the following equation system is obtained from the region D > 0.5:

$$\begin{aligned}\frac{d\tilde{x}}{dt}&=\left[\left(1-D\right)\left(A_{10}+A_{01}\right)+\left(2D-1\right)A_{11}\right]\tilde{x}\\ &\quad+\left[\left(2A_{11}-A_{10}-A_{01}\right)X+\left(2B_{11}-B_{10}-B_{01}\right)V_g\right]\tilde{d}\\ &\quad+\left(\left(1-D\right)B_{10}+\left(1-D\right)B_{01}+\left(2D-1\right)B_{11}\right)\tilde{v}_g\\ y&=\left[\left(1-D\right)\left(C_{10}+C_{01}\right)+\left(2D-1\right)C_{11}\right]\tilde{x}\\ &\quad+\left[\left(2C_{11}-C_{10}-C_{01}\right)X+\left(2D_{11}-D_{10}-D_{01}\right)V_g\right]\tilde{d}\\ &\quad+\left(\left(1-D\right)\left(D_{10}+D_{01}\right)+\left(2D-1\right)D_{11}\right)\tilde{v}_g.\end{aligned} \tag{39}$$

From the averaged models (38) and (39), it is possible to obtain the transfer functions for any of the state variables or the outputs to either the control variable or the input voltage disturbance. For transfer functions related with the control, the input voltage is considered as nule as well as for transfer functions related with the input voltage, the control is considered as nule. For numerical examples, the following transfer functions are considered:

$$G_{vd}(s)=\frac{V_o\left(s\right)}{D\left(s\right)} \tag{40}$$

$$G_{vg}(s)=\frac{V_o\left(s\right)}{V_g\left(s\right)}. \tag{41}$$

The validity of the models is assessed by comparing the response of the complete circuit in a simulated model implemented in PSIM.

B. Numerical Example 1

The parameters defined in Table I corresponding to the numerical example 1 of the previous section were used for this example. Expressions (40)–(41) are evaluated for $v_g = 70$ V, $R = 480\ \Omega$ and $D = 0.425$ obtaining (42) and (43). As it can be noted, there are three roots in the numerator of the transfer function (42) which has a nonminimum phase nature, and two pairs of complex conjugate roots in the numerator of the transfer

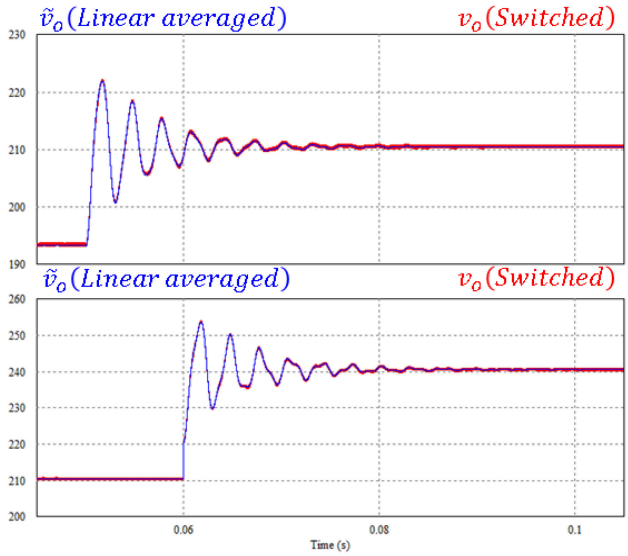

Fig. 13. Comparison of transient responses obtained from the simulation of the complete converter and the averaged model. (a) Increasing stimulus of the duty cycle in the region D<0.5 (0.4 to 0.425). (b) Increasing stimulus of 10 V in the input voltage (D = 0.425).

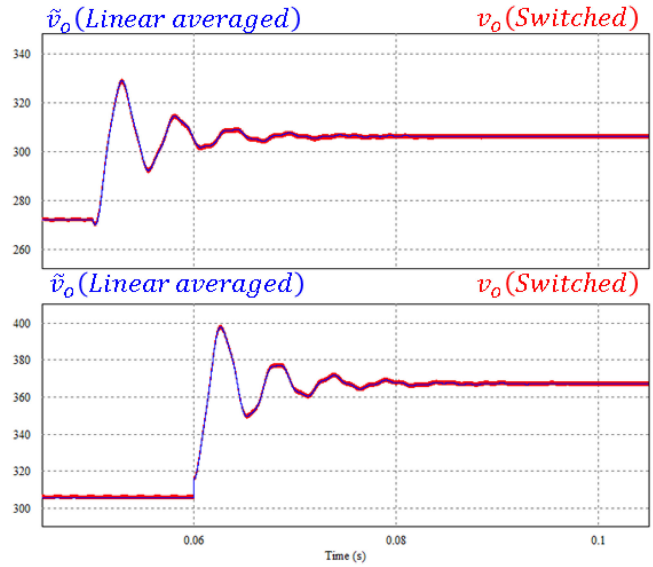

Fig. 14. Comparison of transient responses obtained from the simulation of the complete converter and the averaged model: a) Increasing stimulus of the duty cycle in the region D > 0.5 (0.575 to 0.6); and, b) Increasing stimulus of 10 V in the input voltage (D = 0.575).

function (43).

$$G_{vd}(s) = \frac{-256.9k\,(s-15.61k)\left(s^2+222.1s+15.02M\right)}{\left(s^2+330s+4.1M\right)\left(s^2+216.9s+20.24M\right)} \quad (42)$$

$$G_{vg}(s) = \frac{\left(s^2+40.98s+8.59M\right)\left(s^2+134.5s+29.04M\right)}{\left(s^2+330s+4.1M\right)\left(s^2+216.9s+20.24M\right)}. \quad (43)$$

Fig. 13 shows a comparison of the transient responses obtained from the complete switched circuit simulated and the linearized averaged models (transfer function) in PSIM. First, starting from a duty cycle of 0.4, an increasing stimulus of 0.025 is applied to the duty cycle at 0.05 s. In the same figure, the response of the converter to an input voltage stimulus of 10 V applied at 0.06 s is assessed. The initial input voltage is 70 V for both simulations. The validity of the averaged model for this example is confirmed from time response analysis.

Similarly, (40)–(41) are evaluated for $v_g = 50\,V, R = 480\,\Omega$ and $D = 0.6$ obtaining (44)–(45). In these transfer functions the roots remains in the same region of the complex plane

$$G_{vd}(s) = \frac{-652.1k\,(s-3494)\left(s^2+1247s+12.78M\right)}{\left(s^2+367.6s+1.359M\right)\left(s^2+174.5s+14.5M\right)} \quad (44)$$

$$G_{vg}(s) = \frac{\left(s^2+38.48s+5.98M\right)\left(s^2+130.6s+20.2M\right)}{\left(s^2+367.6s+1.359M\right)\left(s^2+174.5s+14.5M\right)}. \quad (45)$$

Fig. 14 shows the transient responses for the region D > 0.5. Firstly, starting from a duty cycle of 0.6, an increasing stimulus of 0.025 is applied to the duty cycle at 0.05 s. Equally, the response of the converter to an input voltage stimulus of 10 V applied at 0.06 s is assessed. The initial input voltage is 50 V for both simulations. The validity of the averaged model for this example is confirmed from time response analysis.

C. Numerical Example 2

The same procedure applied for the previous example is developed using parameters in Table II. Expressions (40)–(41) were evaluated considering a steady-state starting point with an input voltage of 55 V and a duty cycle of 0.57. The transfer functions (46)–(47) were obtained. As it can be noted, the roots in the complex plane have similar behavior with respect to the numeric example 1

$$G_{vd}(s) = \frac{-714\,(s-11.34k)\left(s^2+1087s+34.54M\right)}{\left(s^2+475.8s+3.878M\right)\left(s^2+451s+44.36M\right)}. \quad (46)$$

$$G_{vg}(s) = \frac{\left(s^2+91.52s+14.15M\right)\left(s^2+4.79s+74.53M\right)}{\left(s^2+475.8s+3.878M\right)\left(s^2+451s+44.36M\right)}. \quad (47)$$

Fig. 15 compares the transient responses obtained from the complete switched circuit simulated in PSIM and the averaged model when a stimulus of 0.03 is applied to the duty cycle at 0.05 s and one of 10 V is applied in the input voltage at 0.06 s. The validity of the model for this example is confirmed from time response analysis.

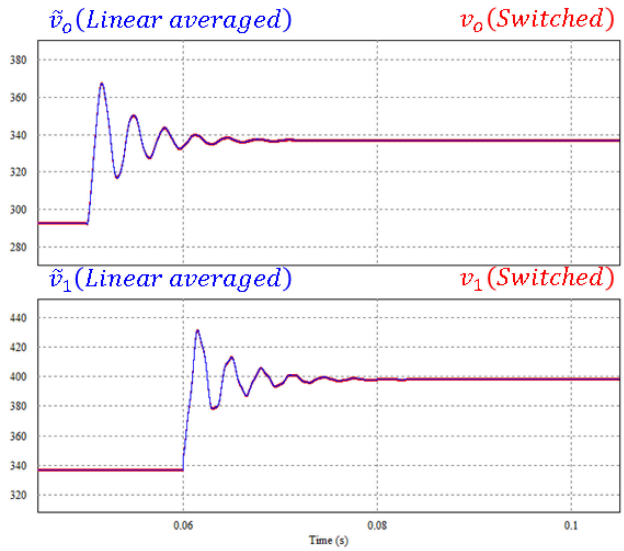

Fig. 15. Comparison of transient responses obtained from the simulation of the complete converter and the averaged model to changes in the duty cycle for numerical example 2: Increasing stimulus in duty cycle from 0.57 to 0.6.

TABLE III
PARAMETERS OF THE CONVERTER PROTOTYPE 1

Element	Symbol	Value	Unities
Capacitor Cell 1	C_1	11	μF
(EPCOS M110725007)	R_{C1}	120	$m\Omega$
Capacitor Cell 2	C_2	11	μF
(EPCOS M110725007)	R_{C2}	120	$m\Omega$
Inductor Cell 1	L_1	270	μH
(Bourns 1140-271-RC)	R_{L1}	100	$m\Omega$
Inductor Cell 2	L_2	810	μH
(Bourns 1140-821-RC)	R_{L2}	200	$m\Omega$
MOSFETs	R_M	120	$m\Omega$
Diodes	R_D	120	$m\Omega$
Switching frequency	f_s	40	kHz
Input voltage	$V_{in_{min}}$	40	V
	$V_{in_{max}}$	60	V
Output voltage	V_o	220	V
Rated power	P_{max}	220	W

IV. EXPERIMENTAL RESULTS

A set of tests were carried out in the laboratory to provide experimental validation to the theoretical predictions with respect to the modeling of the converter. A first converter prototype was build using the passive components listed in Table III as well as two power MOSFET R6020KNZ1 (ROHM), one diode SURF1560 (SMC), and one diode LXA08T600. The gate signals are produced using a dual PWM channel of the DSP TMS320F28335 and optically isolated using two drivers TLP351 whose output side is fed by auxiliary dc sources TRIAD WSU240-1000-13 to entirely isolate the power stage of the control stage. The experimental setup used during measurements for this prototype was composed of one programmable dc source BK Precision XLN6024 and one ITECH Programmable dc Load ITECH IT8512+, taking measurements using one Oscilloscope Tektronix MSO2014B with current probes TCP0020 (see Fig. 16).

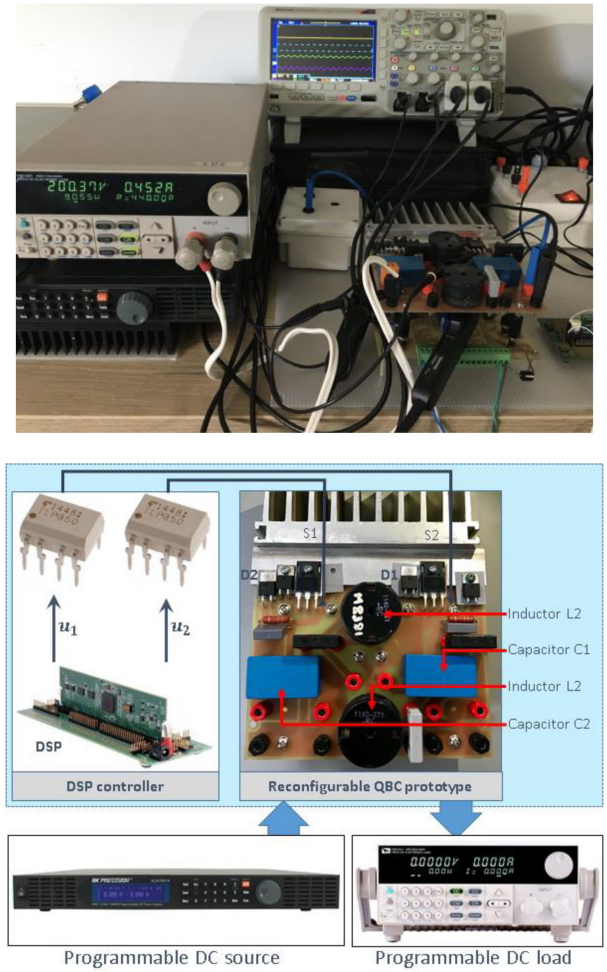

Fig. 16. Photograph of the experimental setup, converter prototype, and instruments.

TABLE IV
PARAMETERS OF THE CONVERTER PROTOTYPE 2

Element	Symbol	Value	Unities
Capacitor Cells 1 and 2	C_1	4.7	μF
(EPCOS M110725007)	R_{C1}	120	$m\Omega$
Inductor Cells 1and 2	L_1	250	μH
(Bourns 1140-271-RC)	R_{L1}	100	$m\Omega$
MOSFETs	R_M	85	$m\Omega$
Switching frequency	f_s	50	kHz
Nominal input voltage	$V_{in_{min}}$	30	V
Nominal output voltage	V_o	250	V
Rated power	P_{max}	400	W

An additional experiment was conducted with a second converter prototype in order to explore the closed-loop behavior and provide efficiency measurements when improved elements are used. The corresponding parameters are listed in Table IV. The prototype uses four gallium nitride (GaN) FET TPH3212PS

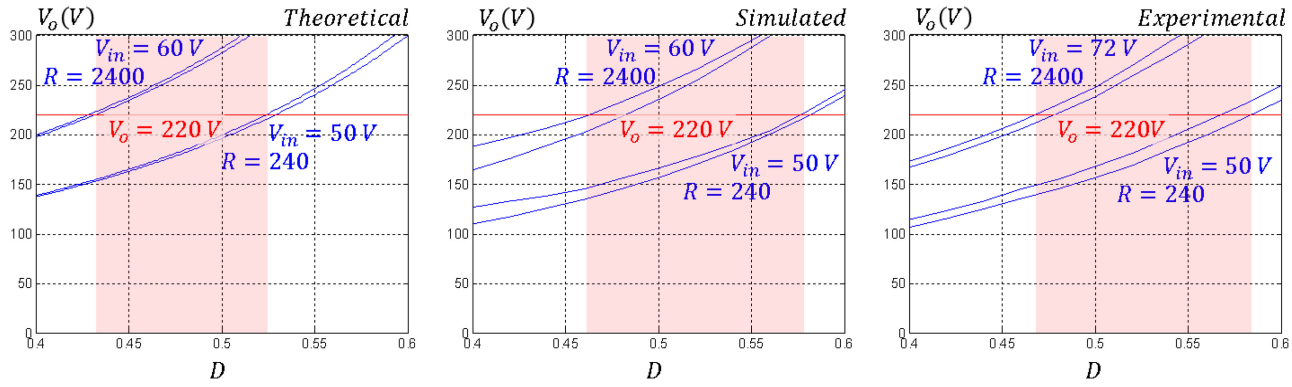

Fig. 17. Comparison of the output voltage to duty cycle curves obtained from theoretical evaluation, simulations, and experiments.

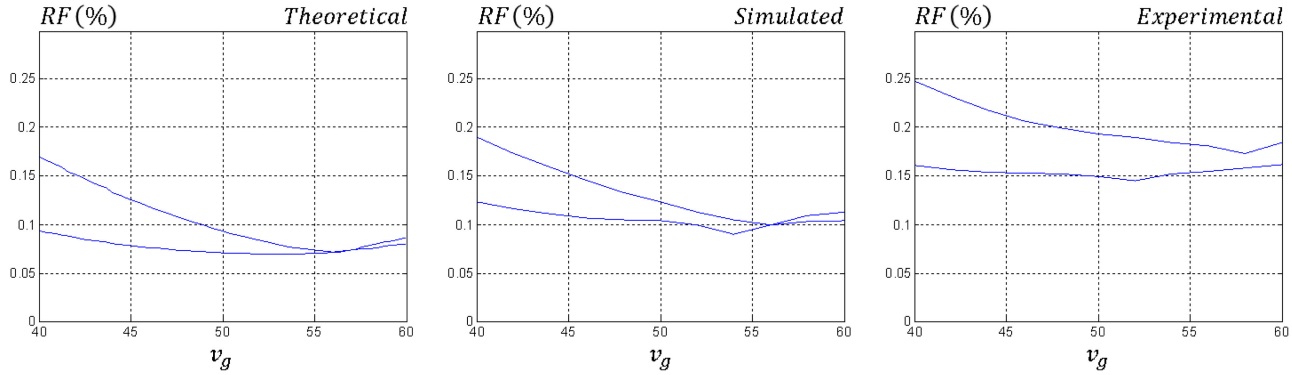

Fig. 18. Experimental measurements of RF as a function of the operation conditions.

(TransPhorm). The gate signals are produced using a dual PWM channel of the DSP TMS320F28335. The experimental setup used was composed of one dc source Keysight de 500V-30A and one BK Precision de 1.5 kW.

A. *Converter Gain Assessment (Prototype 1)*

The gain behavior of the first converter prototype was assessed by comparing the results obtained from theoretical evaluation of the average output voltage with the results obtained from PSIM simulations and laboratory experiments. As it can be observed in Fig. 17 (considering an input voltage between 50 and 60 V, a load resistance between 240 and 2400 Ω, and the objective of 220 V in the output voltage of the converter) the range of duty cycle required for the operation of the converter is higher for both simulation and experiments. The window of variation is around 0.1 for theoretical results while it is around 0.12 for simulation and experiments. The medium point of the range moves to the right from 0.475 to around 0.525. The deviation is mainly due switching losses and other parasitic components that have not been considered in the theoretical modeling approach.

B. *RF Assessment (Prototype 1)*

The RF behavior was evaluated experimentally for a capacitor relation of $C_1 = C_2$, which demonstrated to be the best to operate the converter in a wide range of duty cycle around the point $D = 0.5$. Comparison is developed by assessing the RF for two different levels of output power using: a) the theoretical model; b) the measurement of the RF from PSIM simulations; and c) the measurement of the RF from laboratory experiments. As it can be observed in Fig. 18, the existence of the parasitic resistances in the components increases the optimal RF for different power levels. In addition, with respect to the theoretical model, the results obtained from the simulation of the complete switched circuit shows slightly increased values of the ripple and a small displacement to the right side of the curve (optimal duty slightly increases). Also, experimental results shows a rise in the optimal RF as consequence of spurious phenomena induced by switching events and additional parasitic capacitances and inductances that were not included in models since these effects affect the accuracy of the measurement. In spite of that, the obtained behavior is close to the one obtained from models and simulations.

C. *Steady-State Behavior of the Converter (Prototype 1)*

The waveforms of the converter variables were captured from PSIM simulation and laboratory experiments performing a comparison using the same scales and graphical distribution of signals in the captures. The duty cycle of the converter was adjusted in order to ensure an output voltage of 200 V for four different operations points given by an input voltage (30 or 60 V) and an output load (220 or 440 Ω). As it can be observed in Fig. 19, the current waveforms are practically

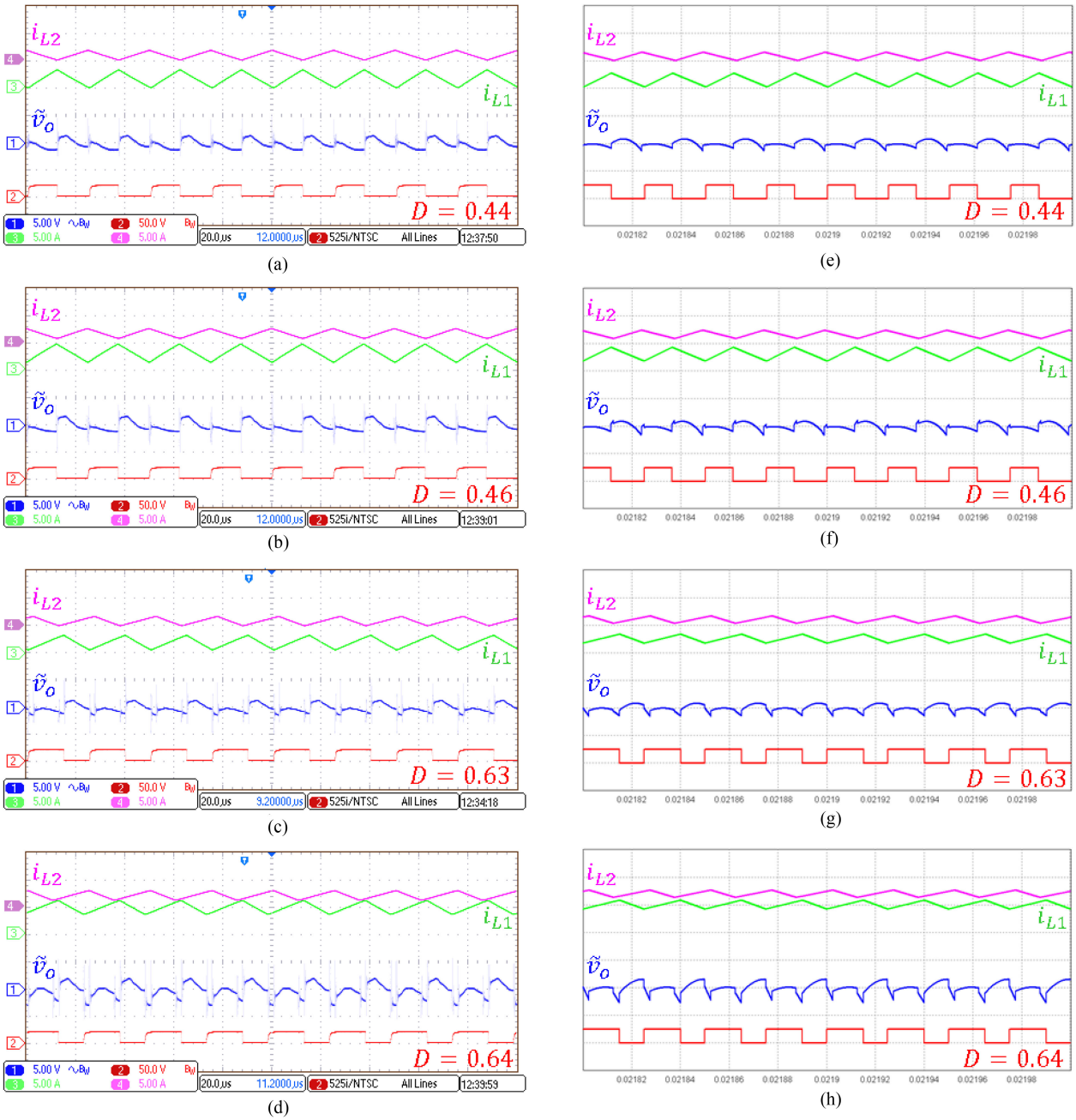

Fig. 19. Comparison of simulated and experimental waveforms. Experiments: (a) Vg = 60 V and R = 440 Ω, (b) Vg = 60 V and R = 220 Ω, (c) Vg = 30 V and R = 440 Ω, and (d) Vg = 30 V and R = 220 Ω. Simulations: (e) Vg = 30 V and R = 440 Ω, (f) Vg = 30 V and R = 220 Ω, (g) Vg = 30 V and R = 440 Ω; and (h) Vg = 30 V, D = 0.4 and R = 220 Ω. Scales of osciclloscope captures: Ch1 (v_o - ac measurement – 5 V/div), Ch2 (v_{gate}- 50 V/div), Ch3 (i_{L1} - 5 A/div), and Ch4 (i_{L2} - 5 A/div).

equal for simulation and experiments, while the ac component of the output voltage shows slight differences mainly related to parasitic capacitances and inductances that has not been included in the models. Despite this, the similarity found is sufficient to support the results presented in this article.

D. Open-Loop Dynamic Response Assessment (Prototype 1)

By using the same set of elements in both cell-type QBC topologies, the open-loop dynamic of the output voltage was compared. For this test, the response to increasing and decreasing step-type stimulus in the duty cycle was assessed. For the experiments, one analog input channel of the DSP was used to modify the duty cycle by means of a symmetric square signal with a frequency of 100 Hz with levels producing changes in the duty cycle from 0.4 to 0.5 and 0.55 to 0.6, then reviewing transient response in both regions of operation of the converter. Two experiments were developed, one starting from a duty cycle below 0.5 and other starting from a duty cycle above 0.5. Both experiments use an input voltage of 30 V and a

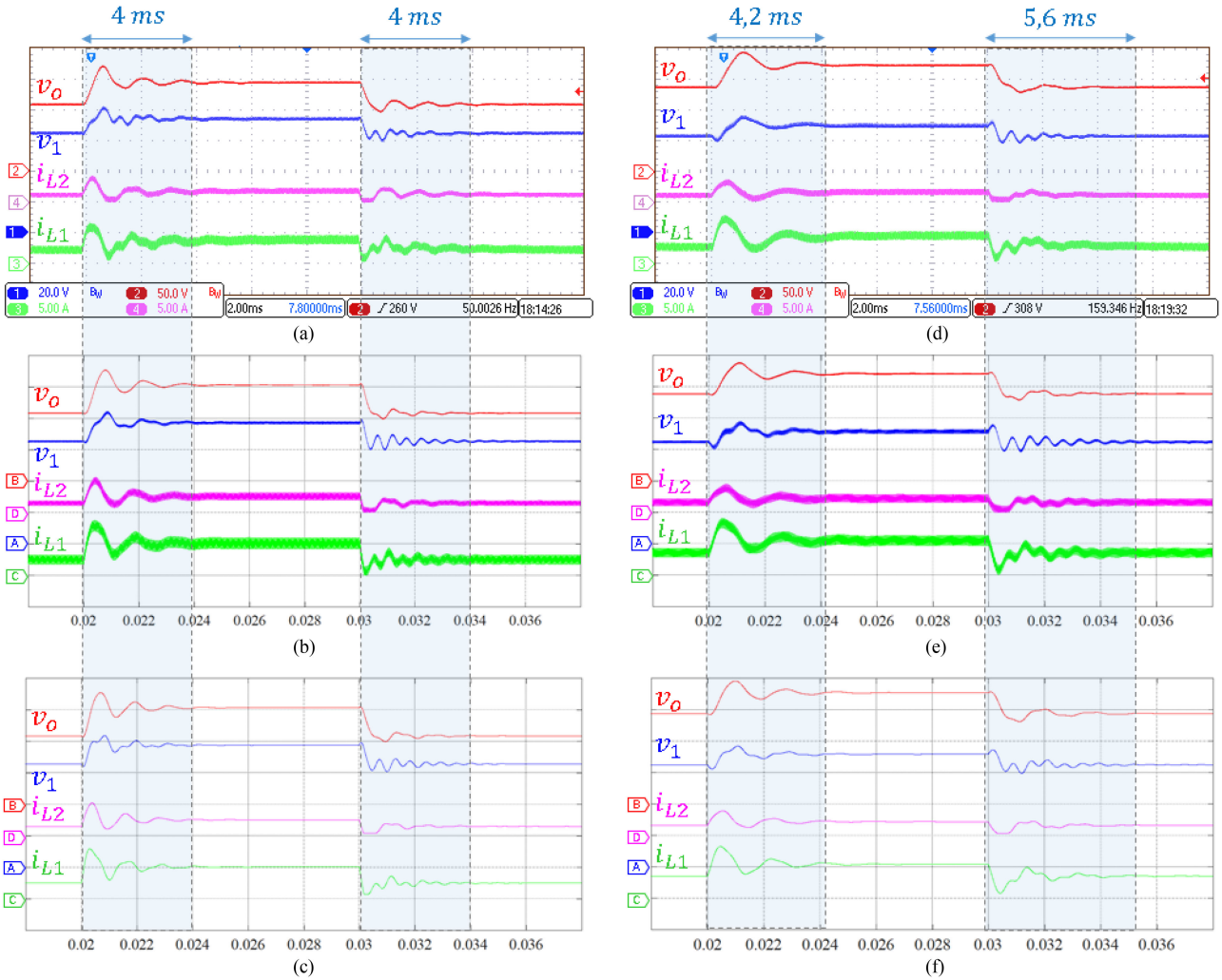

Fig. 20. Time responses of the QBC to duty cycle changes. From 0.4 to 0.5 and vice versa: (a) experimental, (b) simulated switched model, and (c) simulated average model. From 0.55 to 0.6 and vice versa: (d) experimental, (e) simulated switched model, and (f) simulated average model.

load resistance of 440 Ω. Fig. 20 shows a comparison of the transient responses obtained from the nonlinear switched model implemented in MATLAB (subfigures a and b), the linearized averaged model implemented in MATLAB (subfigures c and d) and the real converter (subfigures e and f). Captures obtained from the numerical simulation were adapted to the same scales and configuration of the oscilloscope captures favoring detail in the visual comparison. Time responses with settling times around 20 ms were obtained. The accuracy of the modeling process is confirmed allowing the use of the models for control design.

E. Closed-Loop Dynamic Response Assessment (Prototype 2)

To corroborate the dynamic performance of the converter under closed-loop operation, line and load regulation tests were performed. To do that, a proportional-integral control structure considering a voltage feedback controller was developed to regulate the output voltage to 250 V. The transfer function of the implemented controller is Hs = 0.02 s+363.63/s. As it can be seen in Fig. 21(a), the input voltage is varied from 25 to 35 V and back from 35 to 25 V. It can be observed that the behavior of the capacitor voltages along with the output voltage are well bounded. The same bounded transient behavior is observed in Fig. 21(b) where the load is changed from 150 to 250 W and back to 150 W. In both experiments, the output voltage is well regulated and reaches stability in a maximum time of 10 ms after the transient event.

F. Efficiency Measurement (Prototype 2)

The efficiency of the second power converter prototype was also investigated. A test and computations were performed considering different output power levels and the results are shown in Fig. 22. As can be seen, the converter got maximum efficiencies of 95.8% and 94.3% for the computed and measured value, respectively.

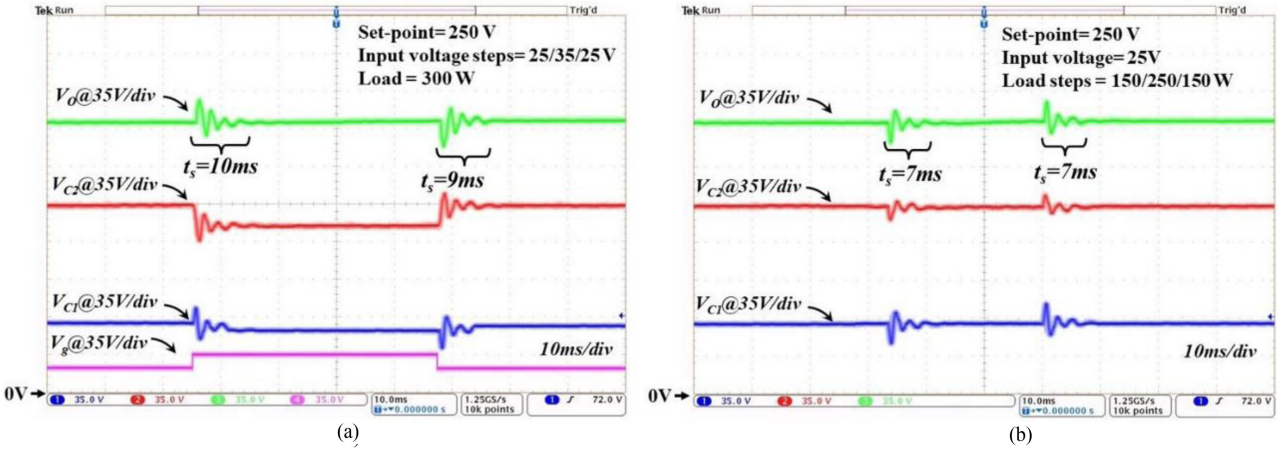

Fig. 21. Closed-loop response of the converter prototype 2. (a) Under input voltage changes from 25 to 35 V. (b) Under output power changes from 150 to 250 W.

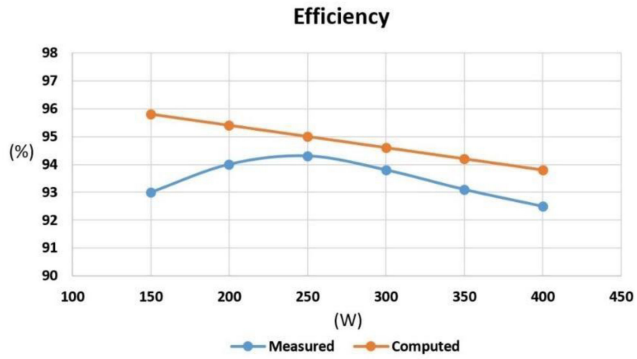

Fig. 22. Measured and computed efficiencies of the converter prototype 2.

V. Conclusion

This article presented a deep and accurate analysis of the LES-QBC operating with constant frequency PWM by regarding its static behavior, including the influence of the parasitic resistances in semiconductors and passive components. The developed analysis has allowed distinguishing two operation regions in the duty cycle, one above and one below the point 0.5. All the waveforms of the converter can be reproduced with high precision using the obtained models. The resulting ripple component in the output voltage was assessed finding that the best region to operate the converter regarding this aspect is around a duty cycle of 0.5. Nevertheless, the advantages of the converter can be exploited in a wide region by using capacitors with reduced ESR such as film capacitors, which is possible with this topology because the value of the required capacitances can be further reduced.

In addition, a linear state-space dynamic model was derived from the analysis of the variable structure behavior of the circuit when a 180° phase displacement is used in the control signals. Although there are differences in the model for the two studied regions, they show a very similar response. The accuracy of the models was confirmed by means of simulation and experimental results. The resulting models can be used for control purposes by applying any classic linear techniques.

The future work related to this research will include the study of the converter and its control to work inside other applications including connection to batteries or dc-buses as loads as well as the use in renewable energy applications.

Appendix 1

According to the state of the control signal u_1, the waveform of the current on the inductor L_1 can be defined as a piecewise function with two time intervals. The expressions for $v_{L1}(t)$ in (1)–(4) can be combined in the generalized form

$$v_{L1}\ (t) = L_1\ \frac{di_{L1}}{dt} = \begin{cases} v_a - i_{L1}R_{E1} & 0 < t < t_a \\ v_b - i_{L1}R_{E1} & t_a < t < T_s \end{cases} \quad \text{(A1)}$$

where $t_a = DT_s$, $v_a = v_g$ and $v_b = v_g - v_1$. The first interval $(0 < t < t_a)$ can be rewritten as follows:

$$L_1 \frac{di_{L1_a}}{dt} + i_{L1_a}\ R_{E1} = v_a. \quad \text{(A2)}$$

By applying the Laplace transform, the following expression is obtained:

$$I_{L1_a}(s) = \frac{\dfrac{V_a}{L_1}}{s\left(s + \dfrac{R_{E1}}{L_1}\right)} + \frac{i_{L1_a}(0)}{s + \dfrac{R_{E1}}{L_1}}. \quad \text{(A3)}$$

By applying the inverse Laplace transform, it is obtained

$$i_{L1_a}(t) = \frac{v_a}{R_{E1}} - \left(\frac{v_a}{R_{E1}} - i_{L1_a}(0)\right) e^{-\frac{R_{E1}}{L_1}t}. \quad \text{(A4)}$$

For the second interval $(t_a < t < T_s)$, the same procedure is applied to obtain

$$i_{L1_b}\ (t) = \frac{v_b}{R_{E1}}\ - \left(\frac{v_b}{R_{E1}} - i_{L1_b}(0)\right) e^{-\frac{R_{E1}}{L_1}t}. \quad \text{(A5)}$$

The inductor current $i_{L1}(t)$ is then described by

$$i_{L1}\ (t) = \begin{cases} \frac{v_a}{R_{E1}} - \left(\frac{v_a}{R_{E1}} - i_{L1_a}\,(0)\right) e^{-\frac{R_{E1}}{L_1}t}\ 0 < t < t_a \\ \frac{v_b}{R_{E1}} - \left(\frac{v_b}{R_{E1}} - i_{L1_b}\,(0)\right) e^{-\frac{R_{E1}}{L_1}t}\ t_a < t < T_s \end{cases}. \tag{A6}$$

To find the initial conditions, the coincidence of the signal sections in the instant t_a is assessed as follows:

$$\frac{v_a}{R_{E1}} - \left(\frac{v_a}{R_{E1}} - i_{L1_a}\,(0)\right) e^{-\frac{R_{E1}}{L_1}t_a} = \frac{v_b}{R_{E1}} - \left(\frac{v_b}{R_{E1}} - i_{L1_b}\,(0)\right) e^{-\frac{R_{E1}}{L_1}t_a}. \tag{A7}$$

By defining that $\gamma = \frac{R_{E1}t_a}{L_1}$ and $\alpha = \frac{v_a - v_b}{R_{E1}e^{-\gamma}} - \frac{v_a - v_b}{R_{E1}}$, it is obtained that

$$i_{L1_b}\ (0) = i_{L1_a}\ (0) + \alpha. \tag{A8}$$

On the other hand, the mean value of $i_{L1}(t)$ can be obtained by definition from (A6) as follows:

$$I_{L1} = \frac{1}{T_s}\left[\int_0^{t_a}\left(\frac{V_a}{R_{E1}} - K_a e^{-\frac{R_{E1}}{L_1}t}\right)dt + \int_{t_a}^{T_s}\left(\frac{V_b}{R_{E1}} - K_b e^{-\frac{R_{E1}}{L_1}t}\right)dt\right] \tag{A9}$$

where $K_a = \frac{V_a}{R_{E1}} - i_{L1_a}(0)$ and $K_b = \frac{V_b}{R_{E1}} - i_{L1_b}(0)$. It is obtained that

$$I_{L1} = \frac{1}{T_s}\left[\frac{(v_a - v_b)\,t_a + v_b T_s}{R_{E1}} - \frac{K_a L_1}{R_{E1}} + \frac{L_1}{R_{E1}}e^{-\gamma}\,(K_a - K_b) + \frac{K_b L_1}{R_{E1}}e^{-\gamma}\right]. \tag{A10}$$

Having that I_{L1} can be obtained from average analysis in (7) or (20), it can be deduced that (A11), shown at the bottom of this page

After that, expression (A8) must be evaluated to complete parameters defining $i_{L1}(t)$ in (A6).

According to the state of the control signal u_2, the waveform of the current on the inductor L_2 can be defined as a piecewise function with three time intervals. The expressions for $v_{L1}(t)$ in (1)–(4) can be combined in a generalized form as follows:

$$v_{L2}\ (t) = L_2\ \frac{di_{L2}}{dt} = \begin{cases} v_a - i_{L1}R_{E1}\ 0 < t < t_b \\ v_b - i_{L1}R_{E1}\ t_b < t < t_c \\ v_a - i_{L1}R_{E1}\ t_c < t < T_s. \end{cases} \tag{A12}$$

For the case of $D < 0.5$, $t_b = 0.5T_s$, $t_c = 0.5T_s(1 + 2D)$, $v_a = v_1 - v_o$, and $v_b = v_1$. For the case of $D > 0.5$, $t_b = 0.5(2D - 1)T_s$, $t_c = 0.5T_s$, $v_a = v_1$ and $v_b = v_1 - v_o$. Then, we have

$$i_{L2}\,(t) = \begin{cases} \frac{v_a}{R_{E2}} - \left(\frac{v_a}{R_{E2}} - i_{L2_a}\,(0)\right) e^{-\frac{R_{E2}}{L_2}t}\ 0 < t < t_b \\ \frac{v_b}{R_{E2}} - \left(\frac{v_b}{R_{E2}} - i_{L2_b}\,(0)\right) e^{-\frac{R_{E2}}{L_2}t}\ t_b < t < t_c \\ \frac{v_a}{R_{E2}} - \left(\frac{v_a}{R_{E2}} - i_{L2_c}\,(0)\right) e^{-\frac{R_{E2}}{L_2}t}\ t_c < t < T_s \end{cases}. \tag{A13}$$

To find the initial conditions, the coincidence of the signal sections in the instants t_b and t_c is assessed as follows:

$$\frac{v_a}{R_{E2}} - \left(\frac{v_a}{R_{E2}} - i_{L2_a}\,(0)\right) e^{-\frac{R_{E2}t_b}{L_2}} = \frac{v_b}{R_{E2}} - \left(\frac{v_b}{R_{E2}} - i_{L2_b}\,(0)\right) e^{-\frac{R_{E2}t_b}{L_2}} \tag{A14}$$

$$\frac{v_b}{R_{E2}} - \left(\frac{v_b}{R_{E2}} - i_{L2_b}\,(0)\right) e^{-\frac{R_{E2}t_c}{L_2}} = \frac{v_a}{R_{E2}} - \left(\frac{v_a}{R_{E2}} - i_{L2_c}\,(0)\right) e^{-\frac{R_{E2}t_c}{L_2}}. \tag{A15}$$

By defining $\gamma_1 = \frac{R_{E2}t_b}{L_2}$, $\gamma_2 = \frac{R_{E2}t_c}{L_2}$, and $\gamma_3 = \frac{R_{E2}T_s}{L_2}$ applying the same solving procedure for differential equations, it is obtained that

$$\frac{v_a - v_b}{R_{E2}e^{-\gamma_1}} - \frac{v_a - v_b}{R_{E2}} = i_{L2_b}\ (0) - i_{L2_a}\,(0) \tag{A16}$$

$$\frac{v_b - v_a}{R_{E2}e^{-\gamma_2}} - \frac{v_b - v_a}{R_{E2}} = i_{L2_c}\ (0) - i_{L2_b}\,(0)\,. \tag{A17}$$

From which, it is defined that $\alpha_2 = \frac{v_a - v_b}{R_{E2}e^{-\gamma_1}} - \frac{v_a - v_b}{R_{E2}}$ and $\alpha_3 = \frac{v_b - v_a}{R_{E2}e^{-\gamma_2}} - \frac{v_b - v_a}{R_{E2}}$. Then

$$i_{L2_b}\ (0) = i_{L2_a}\ (0) + \alpha_2 \tag{A18}$$

$$i_{L2_c}\ (0) = i_{L2_b}\ (0) + \alpha_3 = i_{L2_a}\ (0) + \alpha_2 + \alpha_3. \tag{A19}$$

On the other hand, the mean value of $i_{L2}(t)$ can be obtained by definition from (A13) as follows: Eq. (A20), shown at the top of the next page. where $K_a = \frac{v_a}{R_{E2}} - i_{L2_a}(0)$, $K_b = \frac{v_b}{R_{E2}} - i_{L2_b}(0)$, and $K_c = \frac{v_a}{R_{E2}} - i_{L2_c}(0)$. It is obtained that (A21), shown at the top of the next page.

By replacing K_a, K_b, and K_c, and solving for $i_{L2_a}(0)$, Eq. (A22), shown at the top of the next page, where $K_d = \frac{v_a(T_s + t_b - t_c) + v_b(t_c - t_b)}{R_{E2}}$. Initial conditions $i_{L2_b}(0)$ and $i_{L2_c}(0)$ are obtained from (A18) and (A19), having the complete set of parameters defining $i_{L2}(t)$ in(A13).

$$i_{L1_a}\ (0) = \frac{R_{E1}}{L_1\,(1 - e^{-\gamma})}\left(I_{L1}T_s - \frac{1}{R_{E1}}\left[(v_a - v_b)\,t_a + v_b T_s - \frac{v_a L_1}{R_{E1}} + L_1 e^{-\gamma}\left(\frac{v_a - v_b}{R_{E1}} + \alpha\right) + L_1 e^{-\gamma}\left(\frac{v_b}{R_{E1}} - \alpha\right)\right]\right) \tag{A11}$$

$$I_{L2} = \frac{1}{T_s}\left[\int_0^{t_b}\left(\frac{v_a}{R_{E2}} - K_a e^{-\frac{R_{E2}}{L_2}t}\right)dt + \int_{t_b}^{t_c}\left(\frac{v_b}{R_{E2}} - K_b e^{-\frac{R_{E2}}{L_2}t}\right)dt + \int_{t_c}^{T_s}\left(\frac{v_a}{R_{E2}} - K_c e^{-\frac{R_{E2}}{L_2}t}\right)dt\right] \tag{A20}$$

$$I_{L2} = \frac{1}{T_s R_{E2}}\left(v_a\left(T_s + t_b - t_c\right) + v_b\left(t_c - t_b\right) - L_2\left[K_a + e^{-\gamma_1}\left(K_b - K_a\right) + e^{-\gamma_1}\left(K_c - K_b\right) - K_c e^{-\gamma_3}\right]\right) \tag{A21}$$

$$i_{L2_a}\ (0) = \frac{R_{E2}}{L_2\left(1 - e^{-\gamma}\right)}\left[I_{L2}T_s - \left(K_d - \frac{L_2}{R_{E2}}\left[\frac{v_a}{R_{E2}} + e^{-\gamma_1}\left(\frac{v_a - v_b}{R_{E2}} + \alpha_2\right) + e^{-\gamma_2}\left(\frac{v_b - v_a}{R_{E2}} + \alpha_3\right) + e^{-\gamma_3}\left(\frac{v_a}{R_{E2}} - \alpha_2 - \alpha_3\right)\right]\right)\right] \tag{A22}$$

REFERENCES

[1] F. Lessa Tofoli, D. de Castro Pereira, W. J. de Paula, and D. de Sousa Oliveira Junior, "Survey on non-isolated high-voltage step-up dc–dc topologies based on the boost converter," *IET Power Electron*, vol. 8, no. 10, pp. 2044–2057, 2015.

[2] S. Hasanpour, Y. P. Siwakoti, A. Mostaan, and F. Blaabjerg, "New semi-quadratic high step-up DC/DC converter for renewable energy applications," *IEEE Trans. Power Electron.*, vol. 36, no. 1, pp. 433–446, Jan. 2021.

[3] M. Forouzesh, Y. P. Siwakoti, S. A. Gorji, F. Blaabjerg, and B. Lehman, "Step-Up DC–DC converters: A comprehensive review of voltage-boosting techniques, topologies, and applications," *IEEE Trans. Power Electron.*, vol. 32, no. 12, pp. 9143–9178, Dec. 2017.

[4] L. Qin, L. Zhou, W. Hassan, J. L. Soon, M. Tian, and J. Shen, "A family of transformer-less single-switch dual-inductor high voltage gain boost converters with reduced voltage and current stresses," *IEEE Trans. Power Electron.*, vol. 36, no. 5, pp. 5674–5685, May 2021.

[5] J. C. Rosas-Caro, J. M. Ramirez, F. Z. Peng, and A. Valderrabano, "A DC-DC multilevel boost converter," *IET Power Electron*, vol. 3, no. 1, pp. 129–137, Jan. 2010.

[6] R. W. Erickson and D. Maksimovic, *Fundamentals of Power Electronics*. New York, NY, USA: Springer, 2001.

[7] N. Vazquez, F. Medina, C. Hernandez, J. Arau, and E. Vazquez, "Double tapped-inductor boost converter," *IET Power Electron*, vol. 8, no. 5, pp. 831–840, 2015.

[8] R. Hu, J. Zeng, J. Liu, Z. Guo, and N. Yang, "An ultrahigh step-up quadratic boost converter based on coupled-inductor," *IEEE Trans. Power Electron.*, vol. 35, no. 12, pp. 13200–13209, Dec. 2020.

[9] A. Alzahrani, M. Ferdowsi, and P. Shamsi, "High-Voltage-Gain DC–DC step-up converter with bifold dickson voltage multiplier cells," *IEEE Trans. Power Electron.*, vol. 34, no. 10, pp. 9732–9742, Oct. 2019.

[10] J. C. Rosas-Caro, J. C. Mayo-Maldonado, J. E. Valdez-Resendiz, and A. Valderrabano-Gonzalez, "The resonant DC-DC multilevel boost converter," in *Proc. Int. Conf. Electron., Commun. Comput.*, 2018, pp. 145–151.

[11] J. C. Rosas-Caro, J. C. Mayo-Maldonado, A. Valderrabano-Gonzalez, F. Beltran-Carbajal, J. M. Ramirez-Arredondo, and J. R. Rodriguez-Rodriguez, "DC-DC multiplier boost converter with resonant switching," *Elsevier Electric Power Syst. Res.*, vol. 119, pp. 83–90, Feb. 2015.

[12] D. B. Viet, Y. Lembeye, J. P. Ferrieux, J. Barbaroux, and Y. Avenas, "New high power—High ratio non isolated DC-DC boost converter for fuel cell applications," in *Proc. 37th IEEE Power Electron. Specialists Conf*., 2006, pp. 1–7.

[13] F. S. Garcia, J. A. Pomilio, and G. Spiazzi, "Modeling and control design of the interleaved double dual boost converter," *IEEE Trans. Ind. Electron.*, vol. 60, no. 8, pp. 3283–3290, Aug. 2013.

[14] C. A. Villarreal-Hernandez, J. C. Mayo-Maldonado, G. Escobar, J. Loranca-Coutino, J. E. Valdez-Resendiz, and J. C. Rosas-Caro, "Discrete-time modeling and control of double dual boost converters with implicit current ripple cancellation over a wide operating range," *IEEE Trans. Ind. Electron.*, vol. 68, no. 7, pp. 5966–5977, Jul. 2021.

[15] C. A. Soriano-Rangel, J. C. Rosas-Caro, and F. Mancilla-David, "An optimized switching strategy for a ripple-canceling boost converter," *IEEE Trans. Ind. Electron.*, vol. 62, no. 7, pp. 4226–4230, Jul. 2015.

[16] O. Lopez-Santos, L. Martinez-Salamero, G. Garcia, H. Valderrama-Blavi, and T. Sierra-Polanco, "Robust sliding-mode control design for a voltage regulated quadratic boost converter," *IEEE Trans. Power Electron.*, vol. 30, no. 4, pp. 2313–2327, Apr. 2015.

[17] O. Lopez-Santos, L. Martinez-Salamero, G. Garcia, H. Valderrama-Blavi, and D. A. Zambrano-Prada, "Steady-State analysis of inductor conduction modes in the quadratic boost converter," *IEEE Trans. Power Electron.*, vol. 32, no. 3, pp. 2253–2264, Mar. 2017.

[18] Y. M. Ye and K. W. E. Cheng, "Quadratic boost converter with low buffer capacitor stress" *IET Power Electron*, vol. 7, no. 5, pp. 1162–1170, 2014.

[19] R. Loera-Palomo and J. A. Morales-Saldaña, "Family of quadratic step-up dc–dc converters based on non-cascading structures," *IET Power Electron.*, vol. 8, no. 5, pp. 793–801, 2015.

[20] O. Lopez-Santos, L. Martinez-Salamero, G. Garcia, H. Valderrama-Blavi, and T. Sierra-Polanco, "Comparison of quadratic boost topologies operating under sliding-mode control," in *Proc. Braz. Power Electron. Conf.*, 2013, pp. 66–71.

[21] M. G. Ortiz-Lopez, J. Leyva-Ramos, E. E. Carbajal-Gutierrez, and J. A. Morales-Saldana, "Modelling and analysis of switch-mode cascade converters with a single active switch," *IET Power Electron.*, vol. 1, no. 4, pp. 478–487, 2008.

[22] W. Jiang, S. H. Chincholkar, and C. Chan, "Modified voltage-mode controller for the quadratic boost converter with improved output performance," *IET Power Electron.*, vol. 11, no. 14, pp. 2222–2231, 2018.

[23] F. L. Luo and H. Ye, "Positive output cascade boost converters" *IEE Proc. Elect. Power Appl.*, vol. 151, no. 5, pp. 590–606, 2004.

[24] O. Lopez-Santos, J. C. Mayo-Maldonado, J. C. Rosas-Caro, J. E. Valdez-Resendiz, D. A. Zambrano-Prada, and O. F. Ruiz-Martinez, "Quadratic boost converter with low output voltage ripple," *IET Power Electron.*, vol. 13, no. 8, pp. 1605–1612, 2020.

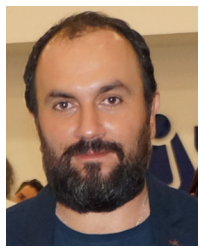

Oswaldo López-Santos (Senior Member, IEEE) received the Electronics Engineer degree from the Universidad Distrital Francisco José de Caldas, Bogotá, Colombia, in 2002, the master's degree in industrial automation from the Universidad Nacional de Colombia, Bogotá, Colombia, in 2011, and the Ph.D. degree from the Institute National des Sciencies Apliquées (INSA) de Toulouse, Toulouse, France, in 2015, developing his research project at LAAS-CNRS.

From 2004 to 2008, he worked in Colombia as a Design Engineer for manufacture of industrial power converters. He is currently an Associate Professor with the Electronics Engineering Department and Leader of the Research Group D+Tec (Technological Development) with the Universidad de Ibagué, Ibagué, Colombia. His current research interests focus on applied control for power electronics.

Dr. López Santos has served as a reviewer for several international journals of IEEE, Elsevier, and Tylor & Francis editorials, among others.

Nicolás López Varón (Student Member, IEEE) received the Electronics Engineer's degree from the Universidad de Ibagué, Ibagué, Colombia, in 2021.

He finished as a Research Assistant with the field of power converters associated to the Research group D+TEC in the Universidad de Ibagué.

Julio C. Rosas-Caro (Senior Member, IEEE) received the B.S. degree in electronics and the M.S. degree in electrical engineering from the Tecnologico de Cd. Madero, Tamps., Mexico, in 2004 and 2005, respectively, and the Ph.D. degree in electrical engineering from the Cinvestav del IPN, Mexico city, Mexico, in 2009.

He has been a Visiting Scholar with the Michigan State University, University of Colorado Denver, and the Ontario Tech. His research interests include power electronics, including dc to dc converters, flexible alternating current transmission system devices, power converter topologies, and applications.

Dr. Rosas-Caro is an Associate Editor of the IEEE LATIN AMERICA TRANSACTIONS. He is currently a Professor with Universidad Panamericana, Mexico city, Mexico.

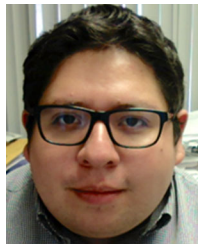

Jonathan C. Mayo-Maldonado (Member, IEEE) received the B.S. and M.Eng. degrees in electrical engineering from Instituto Tecnologico de Ciudad Madero, Ciudad Madero, Mexico, in 2008 and 2010, respectively, and the Ph.D. degree in electrical and electronic engineering from the University of Southampton, Southampton, U.K., in 2015.

From 2015 to 2021 he was a Faculty Member with the Department of Electrical Engineering, Tecnologico de Monterrey, Monterrey, Mexico. He is currently a Lecturer with Electrical Machines and Drives, The University of Sheffield, U.K. His research interests include system and control theory, power electronics, and smart grid technologies.

Dr. Mayo-Maldonado was the recipient of the Doctoral Control & Automation Dissertation Prize 2015 from the Institute of Engineering and Technology (IET), for his thesis entitled "Switched Linear Differential Systems," supervised by Prof. Paolo Rapisarda. He has been an Associate Editor of the Mathematical Problems in Engineering journal since 2020. He is Member of the Sistema Nacional de Investigadores (level 1) in Mexico.

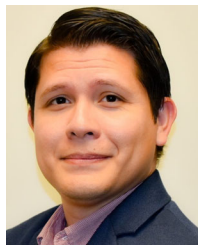

Jesús E. Valdez-Reséndiz (Member, IEEE) received the B.S. and M.Eng. degrees in electrical engineering from the Instituto Tecnológico de Ciudad Madero, Ciudad Madero, Mexico, in 2009 and 2011, respectively, and the Ph.D. degree in electronics engineering from the Centro Nacional de Investigacion y Desarrollo Tecnologico, Cuernavaca, Mexico, in 2015.

He is currently an Associate Professor with the Tecnológico de Monterrey (Campus Monterrey), Monterrey, Mexico. He is a member of the Sistema Nacional de Investigadores, Mexico. His research interests include power electronics, energy management, energy conversion, and electric vehicles.